

## ABSTRACT

### EXPERIMENTS ON ZEEMAN-BASED ELECTROMAGNETICALLY INDUCED TRANSPARENCY AND OPTICAL SENSING IN TURBID MEDIA

by Bradley Worth II

This thesis is divided into two parts. In Part 1 I describe the experimental setup used to investigate electromagnetically induced transparency (EIT). It is shown that impure polarization, stray magnetic fields and imperfect optical alignments cause broadening of the EIT signal and other spurious effects. A systematic approach to minimizing these undesired effects is described, which is shown to produce signals that are four to six times narrower than measurements taken prior to minimization. I conclude part 1 by outlining the progress made toward the production of “slow” light. In Part 2 I describe my earlier research, performed during the first year of my graduate studies, on optical sensing in turbid media. This research culminated in a first accurate measurement of the complex refractive index and in-situ particle sizing in highly scattering opaque media.

EXPERIMENTS ON ZEEMAN-BASED ELECTROMAGNETICALLY INDUCED  
TRANSPARENCY AND  
OPTICAL SENSING IN TURBID MEDIA

A Thesis

Submitted to the

Faculty of Miami University

in partial fulfillment of

the requirements for the degree of

Master of Science

Department of Physics

by

Bradley W. Worth II

Miami University

Oxford, Ohio

2013

*Advisor:* \_\_\_\_\_

(Dr. Samir Bali)

*Reader:* \_\_\_\_\_

(Dr. Perry Rice)

*Reader:* \_\_\_\_\_

(Dr. Burcin Bayram)

# Contents

<b>Introduction to Thesis</b>	1
<b>PART 1</b>	3
<b>1. Electromagnetically Induced Transparency</b>	3
1.1 Motivation	3
1.2 EIT: Fundamental Concepts	3
1.3 Traditional EIT: Conditions for Observation	4
1.4 Zeeman EIT: an Alternative to the Traditional Setup	5
1.5 EIT in Multi-level Atoms	6
<b>2. Setup and Procedure</b>	10
2.1 Initial layout for Observing Zeeman EIT	10
2.2 Noise and EIT Line Broadening Mechanisms	11
2.2.1 Optical Diagnostic for Reducing Noise Contributions from Polarization Impurity, Stray Magnetic Fields, and Misalignments between Optical and Magnetic Fields	12
2.2.2 Reducing Polarization Impurity	13
2.2.3 Minimizing Stray Magnetic Fields	13
2.2.4 Contrast of Spurious Signal; Before and After Improvements	14
<b>3. A Systematic Observation of Zeeman EIT: Results and Discussion</b>	16
3.1 Zeeman EIT Measurements as a Function of Scanning Longitudinal Magnetic Field	16
3.2 Dependence of <sup>85</sup> Rb and <sup>87</sup> Rb EIT Linewidth and Signal-amplitude on Laser Intensity at Zero Transverse Magnetic Field	18
3.3 Dependence of <sup>85</sup> Rb and <sup>87</sup> Rb EIT Linewidth and Signal-amplitude on Transverse Magnetic Field at Fixed Laser Intensity	21
<b>4. Future Outlook and Progress towards Slow Light</b>	25
4.1 Sign Reversal between EIT and EIA	25
4.2 Preliminary results	28

4.3 Introduction to Slow Light	28
4.4 Experimental issues and Progress Achieved	30
4.4.1 New Laser Diode for tuning to the D1 Transitions of Rubidium	30
4.4.2 Oven for Heating Vapor Cell to Increase EIT Signal	31
4.4.3 Creation of Pulsed Light for Demonstration of slowing of Light Pulses	34
 PART 2	 36
<b>5. Optical Sensing</b>	<b>36</b>
5.1 Motivation and Background	36
5.2 Method and Setup	37
5.3 Fresnel Theory and the Corrected Angular Model	38
5.4 Use of Angular Model to Create Accurate Empirical Model of Total Internal Reflection in Highly Turbid Media	40
5.5 Application of our new Model of TIR to in situ Particle Sizing and Biosensing	43
 <b>Appendix A</b>	 45
A.1 Controlling Temperature with Arduino	45
A.2 The Circuit	45
A.3 Arduino Sketch	47
 <b>Refereed Publications as M.S. Co-Author</b>	 49
<b>Oral and Poster Presentations at Miami University</b>	<b>49</b>
<b>Bibliography</b>	<b>50</b>

# List of Tables

5.1	Comparison of Particle-Sizing by AM and F Models for Different Particle Sizes and Concentrations (Size Errors in Columns 6 and 7 are Calculated Relative to the DLS Sizes in Column 3)	43
5.2	The mean size for the suspended oil droplets extracted from our angle-dependent model (AM) is drastically different from the size obtained from traditional Fresnel theory (F). The size error in the last column is the percentage error compared to the size obtained from dynamic light scattering (DLS). The two models also differ significantly in their predictions for $n_r$ , $n_i$ , and $\alpha$ . DLS yields $0.2962\text{ }\mu\text{m}$ for the particle size, within 7% of our result, but disagreeing with the F-model's prediction by almost 40%. Hence we trust our model's in situ sizing capability as well as its predictions for $n_r$ , $n_i$ , and $\alpha$ .	44

# List of Figures

1.1	A) basic three level atomic structure required for EIT. B) Example Transmission spectrum of the EIT signal shown as a peak in probe transmission. Probe laser frequency is swept around the frequency of the coupling laser. Reproduced from reference [7]	4
1.2	A representation showing Zeeman splitting. Note that a state with a total angular momentum of 0 will not split	5
1.3	A) basic three level atomic structure required for EIA	7
1.4	Energy level diagram of $^{85}\text{Rb}$ and $^{87}\text{Rb}$ . Spacing between Hyperfine transitions are denoted in MHz. Note that for both isotopes The only set of transitions which are space more than the Doppler linewidth ( $\sim 500\text{MHz}$ at room temperature) apart are the D1 transitions of $^{87}\text{Rb}$ .	8
1.5	Oscillator strengths of each transition for $^{85}\text{Rb}$ and $^{87}\text{Rb}$ D2 lines. Reproduced from [8]	9
2.1	Initial setup for Zeeman EIT	11
2.2	With just one circularly polarized beam propagating through the cell, a sub-natural line width spectral feature of line width $155\text{kHz}$ is observed. Note that this signal, which falsely suggests EIA, should not have existed in the first place.	12
2.3	Improved layout, as described in section 2.2.2. Note that a quarter waveplate is placed between the vapor cell and the Glan-Thompson polarizer to perform the optical diagnostic test described in Sections 2.2.1-2.2.4	14
2.4	$^{85}\text{Rb}$ , ( $F_g = 2 \rightarrow F_e = 1, 2, 3$ ), shows contrast between the large spurious signal (red) before noise suppression and the minimized spurious signal (blue) after noise suppression, obtained with a single circularly polarized laser beam Note that both signals were taken at the same beam intensity. Note that an EIT signal (peak) is expected on this transition when both $\sigma^+$ and $\sigma^-$ beams are present. Note the red signal is the signal from figure 2.2.	15

- 3.1  $^{85}\text{Rb}$  EIT  $F_g=2 \rightarrow F_e=1,2,3$  transition. For both curves the laser intensity is  $0.42\text{mW/cm}^2$ . For the blue curve the transverse magnetic field is nearly zero ( $< 7$  mG) and the linewidth is measured to be 99kHz. For the orange curve the transverse magnetic field is 1G, and the measured linewidth is 381 kHz, almost 4X broader. 17
- 3.2  $^{85}\text{Rb}$  EIT  $F_g=2 \rightarrow F_e=1,2,3$  transition. For both curves the transverse magnetic field is nearly zero ( $< 7$  mG). For the blue curve the laser intensity is  $0.42\text{mW/cm}^2$  and the measured linewidth is 99kHz. For the orange curve the laser intensity is  $2.1\text{mW/cm}^2$ , and the measured linewidth is 270kHz, almost 3X broader. 17
- 3.3 Width of EIT feature as a function of Beam Intensity, found in  $^{87}\text{Rb}$   $F_g=1 \rightarrow F_e=0,1,2$  transitions. Data taken with the setup in Fig. 2.1 prior to the improvements in Chapter 2 are shown by red triangles, and the data taken with the improved setup in Fig. 2.3 is shown by blue dots. Note that Width is expressed as a function of the Natural linewidth (6MHz for Rb). Transverse magnetic field is set to 0 G. The EIT linewidths measured by the improved setup are consistently a factor  $>7\text{X}$  narrower 18
- 3.4 Peak Height of EIT feature as a function of Beam Intensity, found in  $^{87}\text{Rb}$   $F_g=1 \rightarrow F_e=0,1,2$  transitions. Data taken with the setup in Fig. 2.1 prior to the improvements in Chapter 2 are shown by red triangles, and the data taken with the improved setup in Fig. 2.3 is shown by blue dots. Transverse magnetic field is set to 0 G. The two data sets are practically identical. 19
- 3.5 Width of EIT feature as a function of Beam Intensity, found in  $^{85}\text{Rb}$   $F_g=2 \rightarrow F_e=1,2,3$  transitions. Data taken with the setup in Fig. 2.1 prior to the improvements in Chapter 2 are shown by red triangles, and the data taken with the improved setup in Fig. 2.3 is shown by blue dots. Note that Width is expressed as a function of the Natural linewidth (6MHz for Rb). Transverse magnetic field is set to 0 G. The EIT linewidths measured by the improved setup are consistently a factor 3-5X narrower. 20
- 3.6 Peak Height of EIT feature as a function of Beam Intensity, found in  $^{85}\text{Rb}$   $F_g=2 \rightarrow F_e=1,2,3$  transitions. Data taken with the setup in Fig. 2.1 prior to the improvements in Chapter 2 are shown by red

	triangles, and the data taken with the improved setup in Fig. 2.3 is shown by blue dots. Transverse magnetic field is set to 0 G. The two data sets are practically identical.	21
3.7	Width of EIT feature as a function of transverse magnetic field, found in $^{87}\text{Rb}$ $F_g=1 \rightarrow F_e=0,1,2$ transitions. Data taken with initial setup (Red triangle) and improved setup (Blue dot) Note that Width is in terms of the Natural linewidth. Beam intensity $0.42\text{mW/cm}^2$	22
3.8	Peak Height of EIT feature as a function of transverse magnetic field, found in $^{87}\text{Rb}$ $F_g=1 \rightarrow F_e=0,1,2$ transitions. Data taken with initial setup (Red triangle) and improved setup (Blue dot). Beam intensity $0.42\text{mW/cm}^2$	22
3.9	Width of EIT feature as a function of transverse magnetic field, found in $^{85}\text{Rb}$ $F_g=2 \rightarrow F_e=1,2,3$ transitions. Data taken with initial setup (Red triangle) and improved setup (Blue dot) Note that Width is in terms of the Natural linewidth. Beam intensity $0.42\text{mW/cm}^2$	23
3.10	Peak height of EIT feature as a function of transverse magnetic field found in $^{85}\text{Rb}$ $F_g=2 \rightarrow F_e=1,2,3$ transitions. Data taken with initial setup (Red triangle) and improved setup (Blue dot). Beam intensity $0.42\text{mW/cm}^2$	23
4.1	Illustration of coupling (strong $\sigma^+$ ) and probe(weak $\sigma^-$ ) EIT with orthogonal circular polarizations.	26
4.2	setup for EIT with circular polarized light. Note that quarter waveplates are set such that the coupling beam (blue) and probe beam (red) are orthogonal and circular polarized. Only the probe beam is viewed.	27
4.3	signal observed with 2 orthogonal circular polarized beams when viewing the probe. FWHM of the bump is $\sim 650\text{kHz}$	28
4.4	displays both the index of refraction (red) and the absorption spectrum of EIT (blue) as a function of frequency. Notice the rapid change in the refractive index within the EIT window.	



	Reproduced from [16]	29
4.5	Wavelength dependence on temperature of laser diode. Reproduced from [17]	30
4.6	SAS spectrum for the D1 transitions The lettered peaks are the $^{87}\text{Rb}$ transitions and the numbered peaks are $^{85}\text{Rb}$ transitions. Unlabeled peaks are crossover peaks. Reproduced from [18]	31
4.7	Plot of the density of rubium within the temperature regime we are studying. Data from [19]	32
4.8	observed EIT signals for $^{85}\text{Rb}$ at room temperature, $40^{\circ}\text{C}$ , and $60^{\circ}\text{C}$	33
4.9	Dual AOM setup, used for signal field generation as well as independently regulating the power of the pump and probe fields. (reproduced from [20])	34
5.1	Schematic of home built TIR based refractometer	38
5.2	TIR occurs when $\theta_i > \theta_c$	40
5.3	Reflectance data (1000 datapoints) for aqueous solution of polystyrene spheres (dia $0.356 \pm 0.014 \mu\text{m}$ ). Solid lines are theoretical fits; dots are data. Both the angle-dependent model [dark blue; see text for explanation of spike (bold)] and traditional Fresnel theory (light orange) fit data closely, yet only one is correct.	41
A.1	Circuit diagram for connecting the thermistor to the Arduino. Reproduced from [33]	45
A.2	Diagram depicting how the relay is used to control the power supply to heater. Reproduced from [33]	46

A.3      Image of the Arduino temperature controlling circuit. Note, Pot 1 is the potentiometer used in figure 5 and Pot 2 is used to set the temperature Arduino will maintain.

46

# **Dedication**

To my supportive family, Cherie and Jennifer Worth

In Memory of my father, Bradley Worth (Sr.)

# Acknowledgements

Dr. Samir Bali thanks for all of your time, and help with the project. Dr. Burcin Bayram, thank you for letting us borrow two Glan-Thompson Polarizers as well as a spectrometer. Dr. Herbert Jaeger, thank you for your aid with the initial Arduino setup. Thank you Dr. Perry Rice, for your help in understanding the theory for EIT and slow light. I would also like to thank Jason Barkeloo for my initial mentorship into the EIT experiment and Amanda Day-Wilson for without her Bramanda could never have been conceived. Thank you, Rick Jackson, Kaleb Campell, and Matt van-Vleet, for working with me on the EIT project. Andrew Hachtel, Matt Gillette, Jayampathi Kangaro for sharing your expertise on the laser systems. Kashi Goyal and Miao Dong, thank you for your hard work in data collection and analysis as well as theoretical understanding in the optical sensing lab.

# Introduction to Thesis

This thesis consists of two parts. In the first part – Chapters 1 through 4 – I describe our experimental results in Zeeman-based electromagnetically induced transparency (EIT) and outline progress made toward the production of slow light. In the second part – Chapters 5 through 6 – I describe my earlier research, performed during the first year of my graduate studies, on optical sensing in highly scattering opaque (also known as “turbid”) media. As a Masters’ student I co-authored three research papers based on the turbid media experiments. In order to challenge myself further I decided, mid way during my first summer, to step away from optical sensing since this project had attained a rather mature stage of productivity, and plunge into the Zeeman EIT measurements for which our group is yet to achieve publishable results.

In the Zeeman EIT project my main contributions have been to identify and suppress sources of noise which lead to spurious frequency-broadening of the EIT signals, and initiate modifications in our setup which are necessary to observe slow light in room-temperature rubidium vapor. In the optical sensing project my main contribution was to extend our sensing capability in turbid media to include, for the first time, in situ particle sizing.

The thesis is devoted to describing how these contributions were achieved.

In chapter 1 I describe EIT in a basic three level atomic system. I discuss how EIT is achieved traditionally and in the Zeeman-based EIT configuration. The chapter is concluded by discussing EIT in a multilevel atom, with and without Doppler broadening. The identification and minimization of noise within our setup is discussed in chapter 3. In chapter 4 I show that the noise reduction technique described in Chapter 3 has indeed improved the EIT signal. In chapter 4 I describe the experimental progress we have made toward achieving slow light in our Zeeman EIT setup.

Part 2 is an overview of the work I did on optical sensing in turbid media during the first year as a Master’s student. In Chapter 5 I describe the general principle behind our new empirical model of total internal reflection in turbid media and its application to biosensing. Chapter 6 describes the work accomplished in three recent publications that I co-authored. A complete list of these

publications, and oral presentations made by me at Miami University's Graduate Research Forum, is provided in Appendix 2 of the thesis.

# Part 1

## Chapter 1

### Electromagnetically Induced Transparency

#### 1.1 Motivation

In recent years, progress in the development of new quantum information and sensors technologies as well as improvement of existing technologies has been dramatically improved by use of the phenomenon known as electromagnetically induced transparency (EIT).[1] Such improvements include increased precision of atomic clocks[2] and sensitive magnetometers.[3,4] There are new fundamental effects such as “production of ultraslow light”, made possible by the fact that EIT is often accompanied by a million-fold increase in refractive index of the atomic vapor.[5] New technologies in the field of quantum information are currently being pursued, such as “building of quantum memory” where quantum properties of light are stored as spin excitation in an atomic medium to be released at will.[6]

Our main goal in this thesis is to seek an experimental understanding of EIT and produce clean signals in a setup that is significantly simpler than the traditional EIT experiments. We also wish to initiate an experimental investigation into the feasibility of producing “slow light” in our lab. Besides the pedagogical benefits of carrying out EIT research in undergraduate-friendly experimental setups, preliminary evidence suggests that our simplified setup yields EIT signals on atomic hyperfine transitions for which such signals were previously thought to be inaccessible owing to their exceedingly small signal-to-noise ratio.

#### 1.2 EIT: Fundamental Concepts

Consider the three level atom shown in fig. 1.1A ( $\Lambda$ -system). Here two close-lying ground states,  $|g_1\rangle$  and  $|g_2\rangle$ , are excited to a common upper-energy level  $|e\rangle$  by two lasers of frequencies  $\omega_1$ , and  $\omega_2$ . These lasers are resonant with the transitions  $|g_1\rangle \rightarrow |e\rangle$  and  $|g_2\rangle \rightarrow |e\rangle$  respectively. In quantum mechanics, it is known that when two or more equally likely paths lead to the same final state, the probability amplitudes of those paths may interfere. In the case of our

three level atom, the probability amplitudes of the two paths,  $|g_1\rangle \rightarrow |e\rangle$  and  $|g_2\rangle \rightarrow |e\rangle$  can destructively interfere under certain conditions. When this happens, absorption from either laser can no longer occur. At this point the atom is said to be in a “dark state” – a non absorbing superposition of the ground states – and becomes transparent to both laser fields. This effect is known as Electromagnetically Induced Transparency (EIT).

A

B

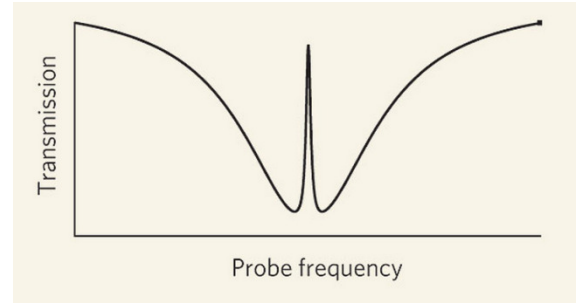
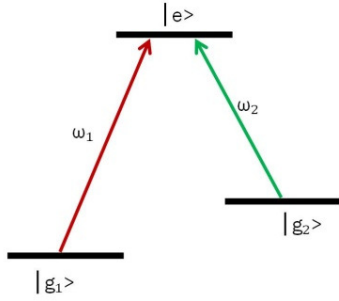


Figure 1.1: A) basic three level atomic structure required for EIT. B) Example Transmission spectrum of the EIT signal shown as a peak in probe transmission. Probe laser frequency is swept around the frequency of the coupling laser. Reproduced from reference [7]

The EIT signal appears as a narrow peak as seen in figure 1.1B. The peak arises from coherent stimulated emission process inside the atom and hence has a linewidth much narrower than the natural linewidth. This graph is created by keeping  $\omega_1$  locked (commonly referred to as the “coupling” frequency) while  $\omega_2$  (the “probe”) is swept about  $\omega_1$ . The probe transmission spectrum is shown. The EIT signal peaks when the probe detuning from the coupling laser is zero, because then the two excited pathways from  $|g_1\rangle \rightarrow |e\rangle$  and  $|g_2\rangle \rightarrow |e\rangle$  are identical thus maximizing interference.

### 1.3 Traditional EIT: Conditions for Observation

To achieve EIT experimentally probe and coupling beams must be perfectly co-aligned, mode matched, and phase-locked for optimal signal. In particular without phase-locking, the lasers would not give rise to coherent processes such as EIT. The coupling field has a fixed frequency while the probe field is frequency-swept around the coupling frequency. The probe transmission spectrum is recorded, and narrow spectral features, most likely signifying EIT, are observed.



### 1.4 Zeeman EIT: An Alternative to the Traditional Setup

In this case, EIT can be achieved using only a single laser source, eliminating the need to phase-lock two separate lasers. Here a magnetic field is used to sweep the Zeeman sub levels of an atomic vapor, effectively scanning the frequency of any laser passing through. A linearly polarized laser passes through the atomic vapor propagating in the same direction as the applied magnetic field. This magnetic field causes a Zeeman splitting, shown in figure 1.2 for the case of a simple two level system  $F_g = 1 \rightarrow F_e = 0$ , where  $F$  is the hyperfine quantum number denoting the total angular momentum of the atom (electron orbital and spin angular momentum, and nuclear spin). The applied magnetic field creates three ground states,  $m_{Fg} = 1, 0, +1$ . The  $+1$  and  $-1$  ground states raise and lower, respectively by an amount that is linearly proportional to the magnitude of the magnetic field. The zero levels in the ground and excited states do not shift.

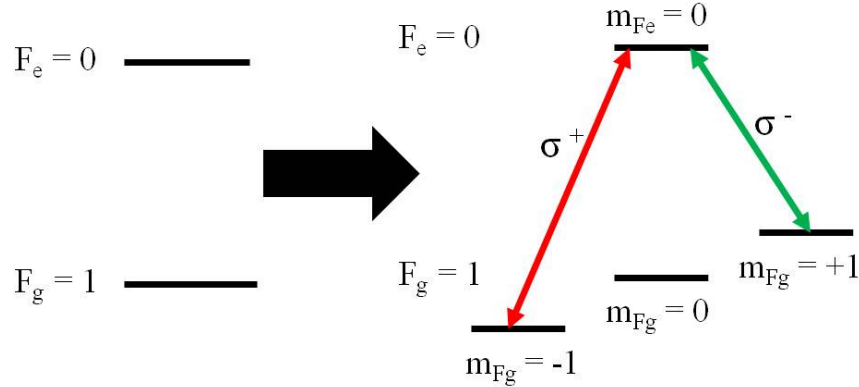


Figure 1.2: A representation showing Zeeman splitting. Note that a state with a total angular momentum of 0 will not split.

The main advantage of using this setup is that it is possible to employ one linearly polarized laser rather than two lasers described in the traditional EIT setup. If the direction of the magnetic field is chosen as usual to be the quantization axis, then the single linearly polarized beam acts as a superposition of left and right circularly polarized beams, effectively creating a pair of phase-locked, collinear beams that can be treated as the pump-probe pair.

However there are three disadvantages inherent in the single-beam Zeeman EIT setup. First, it is important to note that both the pump and probe beams are swept in frequency, when the original intent was to scan just the probe. This complicates our attempts to theoretically

understand the observed signal. Second, the theory is complicated by the fact that Zeeman splitting of the hyperfine structure in rubidium consists of a multitude of energy levels. Third, the relative intensities of the two circular polarized beams cannot be changed because the experimenter does not have separate access to either beam. Despite these disadvantages, single-beam Zeeman EIT is appealing to experimenters because the lab setup is simple, while still allowing sophisticated access to EIT-related phenomena. In the sections below, and in Chapters 2 and 3, we describe our results obtained with this single beam version of Zeeman EIT. In Chapter 4 we point out a simple method to break away from the single beam version of Zeeman EIT described above, is to employ two separate circularly polarized beams. Both these beams are derived from the same laser, hence are still automatically phase-locked. However, the third “disadvantage” referred to above in the single-beam version of Zeeman EIT, namely the inability to separately access each of the two beams, is circumvented.

### 1.5 EIT in Multi-level Atoms

In real multi-level atoms the situation is far more complex than is shown in figure 1.2. For example, in  $^{85}\text{Rb}$ , the values for  $F_g$  could be 2 or 3 and values for  $F_e$  could be 1,2,3, or 4. With this more complex system how can we use our previous understanding of EIT to predict if EIT should be seen at all? To fully appreciate these complex systems one must consider the sister effect of EIT known as Electromagnetically Induced Absorption (EIA). In the case of a three level atom (figure 1.3) where now two excited states share a common ground level, quantum interference can destructively interfere between the probability amplitudes for stimulated emission from the two driven transitions. When destructive interference happens the atom can no longer be stimulated down to the ground state and instead relaxes via spontaneous emission. In other words, in EIA stimulated emission is redirected as spontaneous emission. This process appears as a dip in the transmission spectrum of the laser or conversely a peak in absorption spectrum.

In a multi level system both EIT and EIA may be occurring simultaneously. Which process dominates can be illustrated simply by viewing the EIT structure as a  $\Lambda$  (lambda) system and EIA as V (vee) system. When predicting whether a transition should yield EIT or EIA there are three cases to consider. First, there may be more lower magnetic sublevels than upper sublevels, i.e.,  $m_{F_g} > m_{F_e}$ . Second, there may be the same number of upper and lower magnetic sublevels, i.e.,  $m_{F_g} = m_{F_e}$ . Finally, there may be more upper magnetic sublevels than lower

sublevels, i.e.,  $m_{Fg} < m_{Fe}$ . In the first case more  $\Lambda$  systems exist therefore an overall EIT signal will be observed. In the third case the opposite is true, there are more V systems and therefore an EIA will be viewed. The second case is a bit more tricky as there are an equal number of  $\Lambda$  and V systems. However an overall EIT is observed because in the V system spontaneous emission weakens the dark state while in the  $\Lambda$  case spontaneous emission plays no role since the atoms are “stuck” in the ground state. This means that the  $\Lambda$  system dominates over the V system.

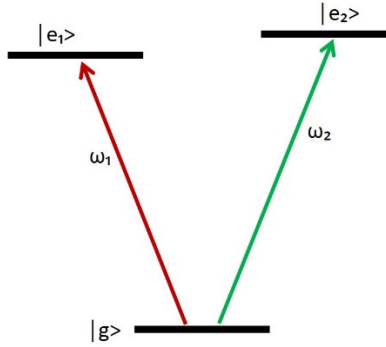


Figure 1.3: Basic three level atomic structure required for EIA.

However we still do not have the complete story. In reality when we have our laser tuned to a particular hyperfine transition, we end up exciting other close lying hyperfine transitions. In fact, it is impossible to only excite one hyperfine transition without eliminating the  $\sim 500\text{MHz}$  Doppler linewidth of Rb as Illustrated in figure 1.4

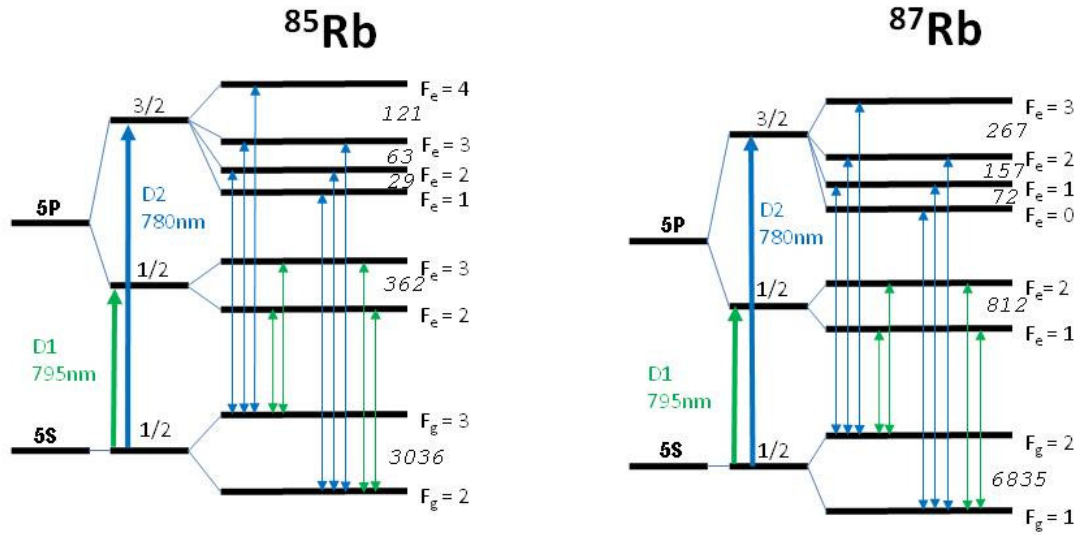


Figure 1.4: Energy level diagram of  $^{85}\text{Rb}$  and  $^{87}\text{Rb}$ . Spacing between hyperfine transitions are denoted in MHz. Note that for both isotopes the only set of optical transitions which are spaced apart more than the Doppler linewidth ( $\sim 500\text{MHz}$  at room temperature) are the D1 transitions of  $^{87}\text{Rb}$ .

Consider the laser tuned near resonance with the  $F_g = 3 \rightarrow F_e = 4$  transition in  $^{85}\text{Rb}$ . Note that the laser is not far from resonance with the neighboring hyperfine transitions  $F_g = 3 \rightarrow F_e = 2, 3$ . Based on the logic of whether there are more upper or lower ground magnetic sublevels we would predict EIT for the  $F_g = 3 \rightarrow F_e = 2$  and  $F_g = 3 \rightarrow F_e = 3$  transitions, and conversely EIA for the  $F_g = 3 \rightarrow F_e = 4$  transition. Due to the simultaneous excitation of all three hyperfine transitions  $F_g = 3 \rightarrow F_e = 2, 3, 4$  one may ask, what is the net effect? The answer depends on the relative strengths of the  $F_g = 3 \rightarrow F_e = 2, 3, 4$  transitions. The oscillator strengths for each transition in  $^{85}\text{Rb}$  and  $^{87}\text{Rb}$  are shown in fig.1.5. In the case of the  $F_g = 3 \rightarrow F_e = 2, 3, 4$  transition in  $^{85}\text{Rb}$  we see that the  $F_g = 3 \rightarrow F_e = 4$  is stronger than the sum of  $F_g = 3 \rightarrow F_e = 2, 3$ . Therefore we expect the net effect from exciting  $F_g = 3 \rightarrow F_e = 2, 3, 4$  transition to be an EIA.

Consider another example  $^{85}\text{Rb}$   $F_g = 2 \rightarrow F_e = 1, 2, 3$ . The  $F_g = 2 \rightarrow F_e = 1$  transition would yield an EIT feature, as would the  $F_g = 2 \rightarrow F_e = 2$  transition, while the  $F_g = 2 \rightarrow F_e = 3$  transition would yield EIA. From fig.1.5.2 we see that the sum of the strengths of  $F_g = 2 \rightarrow F_e = 1$  and  $F_g = 2 \rightarrow F_e = 2$  is greater than  $F_g = 2 \rightarrow F_e = 3$ , thus yielding a net EIT for the  $^{85}\text{Rb}$   $F_g = 2 \rightarrow F_e = 1, 2, 3$  transitions.

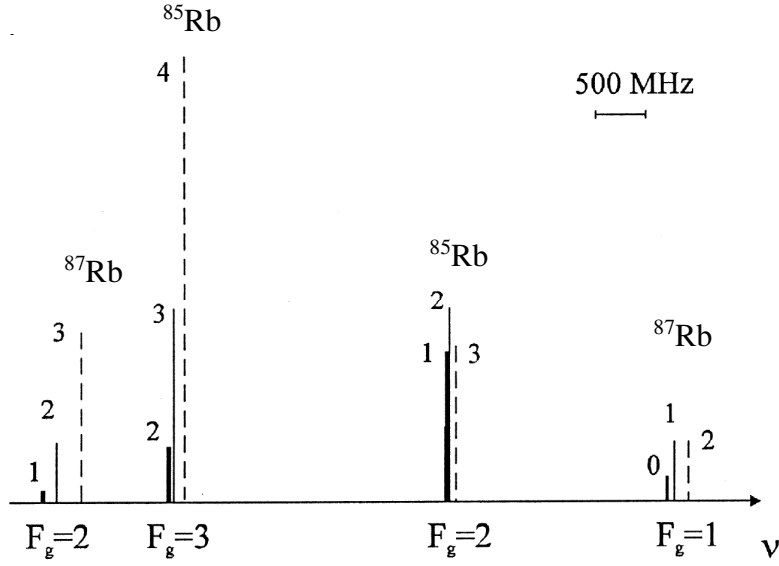


Figure 1.5: Oscillator strengths of each transition for  $^{85}\text{Rb}$  and  $^{87}\text{Rb}$  D2 lines. Reproduced from [8]

Now that I have elucidated the working principles of EIT, I will describe in the following chapter how we are able to achieve EIT experimentally in the lab. I will also discuss how one can suppress spurious signals caused by polarization impurity, and misalignments between the axes of the optical and magnetic fields.

# Chapter 2

## Setup and procedure

In this chapter I will discuss the experimental apparatus we used to achieve EIT. I will also discuss noise sources which lead to false EIT signals and how we suppress these noise-contributions.

### 2.1 Initial Layout for Observing Zeeman EIT

The D2 transitions of  $^{85}\text{Rb}$  and  $^{87}\text{Rb}$  (see Fig. 1.5) are our transitions of choice for studying EIT because the D2 lines yield larger signals than the D1 lines. Furthermore, diode lasers capable of exciting D2 transitions are readily available from Dr. Bali's Cold Atom lab. Figure 2.1 shows the Zeeman EIT layout used. Starting from the right we use an external cavity diode laser (ECDL) which is frequency locked using the saturated absorption spectrum of the Rubidium D2 lines. Exiting the ECDL the beam is of an elliptical shape. The beam passes through the anamorphic prism pair which reshapes the beam such that it has a Gaussian profile. The beam then passes through an optical isolator which acts as a one-way valve for light. This prevents unwanted back reflections into the laser cavity. Next the beam's height from the table is adjusted using the M1 mirrors before being magnified using a telescope arrangement comprising a 4x objective and 5cm diameter lens. We use an iris to select a clean part of the magnified beam. This is then collimated and sent through a polarizing beam splitter. Horizontally polarized light passes through while vertically polarized light is blocked (directed to a beam dump BD). The horizontally polarized beam then passes through a beam splitter and is directed by three mirrors (M2), used to adjust height and position of the beam, through the vapor cell. With an infrared card, we check to make sure that the beam is centered through the entire length of the cell. This is adequate for preliminary measurements. The cell itself is wrapped in a solenoid in which the current is ramped at 3.2Hz thus producing a longitudinal scanning magnetic field of  $\pm 21.5$  Gauss. The probe's transmitted intensity is then viewed by a photodiode, and is plotted as a function of the scanning longitudinal magnetic field. The magnetic field is converted to a

frequency using 0.47MHz/Gauss for  $^{85}\text{Rb}$  EIT transitions and 0.7MHz/Gauss for  $^{87}\text{Rb}$  EIT transitions.

Polarization purity of the beam into the vapor cell was measured to be 98% -99% pure. (we found later that this purity was not good enough.) Using a state of the art magnetometer, Sypris 730, the Helmholtz coils were set such that all magnetic fields canceled in the center of the coils to within 7 milligauss. The solenoid-wrapped vapor cell is placed inside the Helmholtz coils and the laser is aligned along its central axis. This alignment needs further refinement based on an optical diagnostic described later in sections 2.2.2 - 2.2.3.

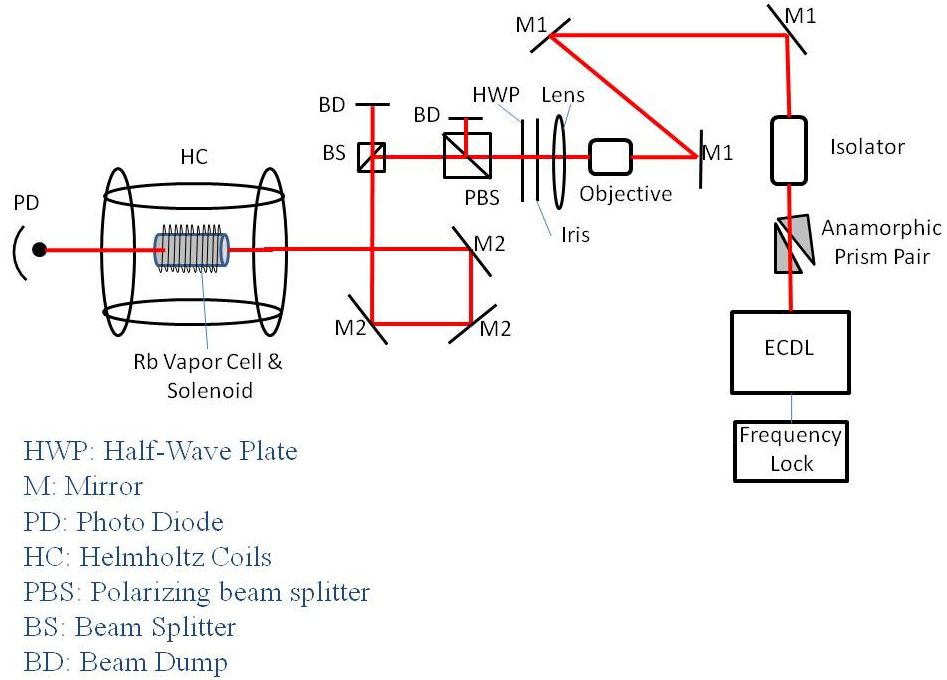


Figure 2.1: Initial setup for Zeeman EIT

## 2.2 Noise and EIT Line Broadening Mechanisms

While we have achieved EIT with the setup described in Sec. 2.1 the measured width of the signal has been on the order of a few hundred kHz. Widths observed by other groups are on the order of kHz [1,9]. We suspect that there are noise induced broadening mechanisms at play in our setup. Possible sources of noise and broadening are small magnetic fields which are

undetectable by our gauss meter, small amounts of polarization impurity, slight misalignments in beam alignment through both the center of solenoid and Helmholtz coils, as also misalignment of the solenoid axis with the axes of the Helmholtz coils. Below I describe a simple optical diagnostic we introduced that we found very useful in identifying and suppressing these undesirable contributions.

### 2.2.1 Optical Diagnostic for Reducing noise contributions from Polarization Impurity, Stray Magnetic Fields, and Misalignments Between Optical and Magnetic Fields

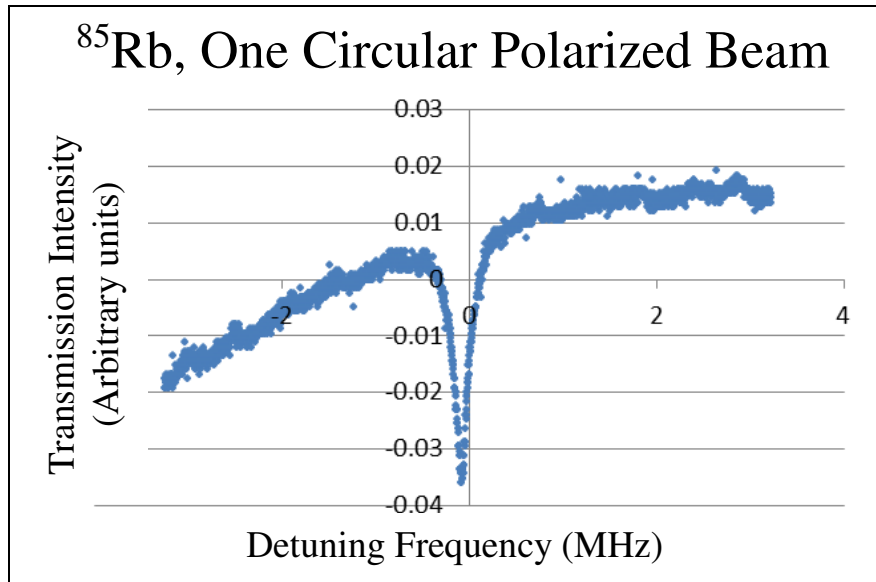


Figure 2.2: With just one circularly polarized beam propagating through the cell, a sub-natural line width spectral feature of line width 155kHz is observed. Note that this signal, which falsely suggests EIA, should not have existed in the first place.

In order to check for artifacts caused by polarization impurity and/or stray magnetic fields, we decided to create a single circular polarized beam prior to the vapor cell, using a quarter waveplate. As is clear from figure 1.1 with just one circular polarization no  $\Lambda$  system can be created and therefore no sub-natural linewidth features should be observed. The observed transmission spectrum of this single  $\sigma$ - polarized beam, showing an unexpected spectral feature of sub-natural linewidth, is shown in fig.2.2. The cause of this spurious sub-natural spectral feature is due to polarization



impurity and stray magnetic fields. In the following section I discuss our attempt to suppress these contributions. It is crucial for EIT experiments to obtain extremely high polarization purity (at the  $10^{-5}$  level) [10], extremely low residual magnetic fields (less than a few mG), and extremely good alignment between the laser beam propagation and the magnetic fields from the solenoid and Helmholtz coils.

### **2.2.2 Reducing Polarization Impurity.**

As stated previously, light reflected off the mirrors are roughly 98% pure. The first thing we did was remove the last three mirrors (M2) prior to the vapor cell in Fig. 2.1. After investigating the polarizers, we found that their purity, i.e. rejection ratio, was at the  $10^{-3}$  level. This level of purity is not good enough for EIT [11]. The improved setup is shown in figure 2.3. We replaced the polarizers with Glan-Thompson polarizers with purity at the  $10^{-5}$  level. They are the last optical component to be placed before the vapor cell to ensure the required polarization purity. This step causes significant reduction of the spurious signal in figure 2.2.

### **2.2.3 Minimizing Stray Magnetic Fields**

The Helmholtz coils are used to zero out the earth's magnetic field along the length of the vapor cell. In the past it was standard practice to use a state of the art gauss meter (Sypris 730). This method is highly intrusive to the setup as it requires each time that the vapor cell be removed causing optical misalignments to ensue. Instead we set the system up such that the spurious EIT signal from a single circular probe beam is being viewed on an oscilloscope. We then change the current through the Helmholtz coils until the spurious signal is minimized.

Not only is it important to minimize the stray magnetic fields but it is also crucial to ensure that the laser beam passes accurately through the center of the vapor cell such that the laser is co-axial with the solenoid axis and the Helmholtz coils' axes. To do this we make slight adjustments to the beam height (unnoticeable to the human eye) and attempt to further minimize the spurious signal in figure 2.2. Occasionally it may be necessary to slightly move the vapor cell itself. This new all-optical method of alignment is much more reliable. Previously we were bound by the reliability of measurement tools such as the gauss meter for magnetic field measurements and rulers to find the center of

the cell - these two approaches left too much room for an accumulation of seemingly minor errors to propagate through the setup.

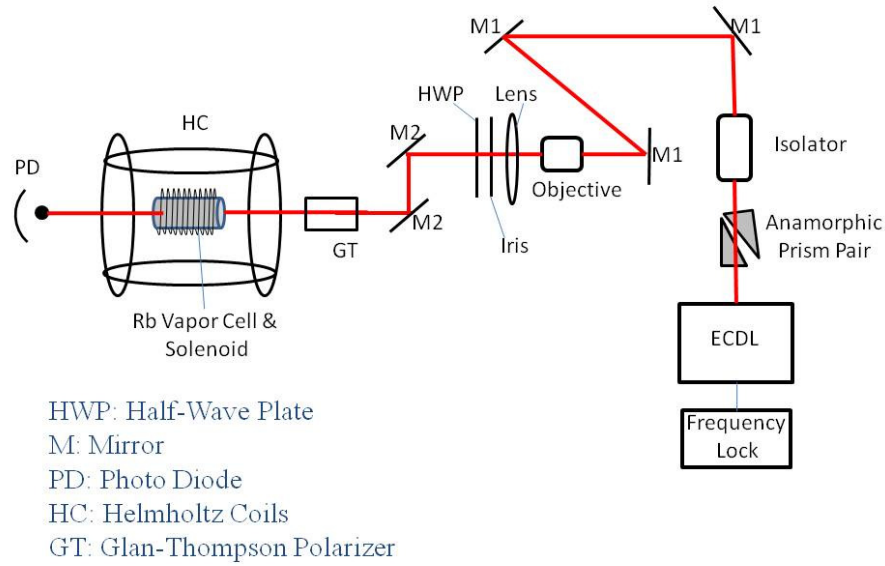


Figure 2.3: Improved layout, as described in section 2.2.2. Note that a quarter waveplate is placed between the vapor cell and the Glan-Thompson polarizer to perform the optical diagnostic test described in Sections 2.2.1-2.2.4

## 2.2.4 Contrast of Spurious Signal; Before and After Improvements

Figure 2.4 shows the new minimized signal (blue data) obtained from the setup in Figure 2.3, plotted with the initial spurious signal (red data) obtained from the setup in Figure 2.1. Clearly the size of this spurious sub-natural linewidth spectral feature depends sensitively on the alignments. The painstaking effort in increasing the polarization purity and minimizing stray magnetic fields, while improving optical alignment has reduced the size of the spurious signal by nearly a factor four. The shape of this spurious signal varies after each detailed alignment procedure, typically taking on either the shape shown or a more dispersive-like shape. But, if the alignments are good, the overall size stays more or less the same as shown in Fig. 2.4 or less.

There could be several reasons for the existence of the residual small spurious signal in Figure 2.4 (blue curve). Small unavoidable amounts of polarization impurity result from passage through the optical window of the glass vapor cell. Furthermore,

some misalignment between the axes of the solenoid and the Helmholtz coils always remains.

One may argue that the reduced spurious signal size may also arise from *misalignments* instead of improved alignment. The answer is to make detailed EIT measurements with the improved setup and compare our results with measurements made on the previous setup. In the following chapter I will show that we have indeed improved the setup by comparing my EIT measurements on the new setup with those taken by a previous graduate student on the old setup.

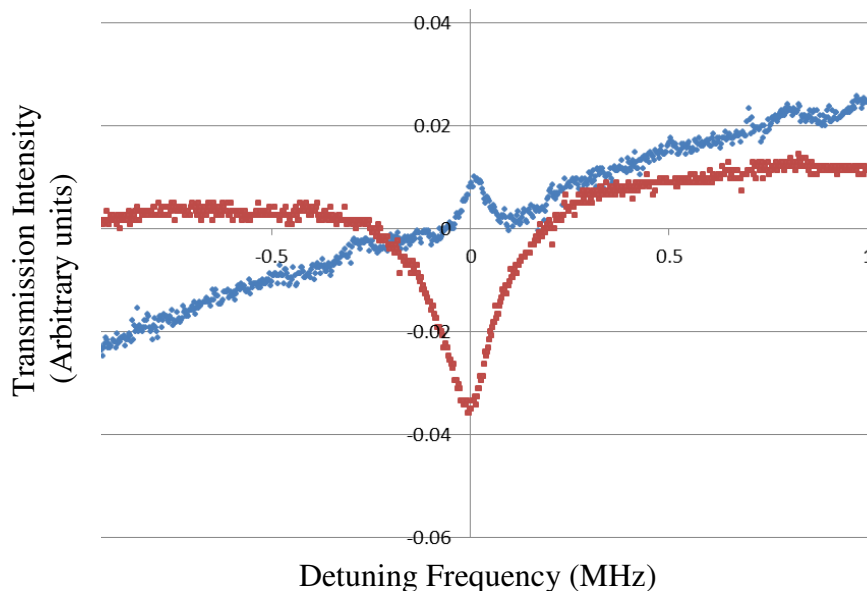


Figure 2.4:  $^{85}\text{Rb}$ , ( $F_g=2 \rightarrow F_e=1,2,3$ ), shows contrast between the large spurious signal (red) before noise suppression and the minimized spurious signal (blue) after noise suppression, obtained with a single circularly polarized laser beam. Note that both signals were taken at the same beam intensity. Note that an EIT signal (peak) is expected on this transition when both  $\sigma^+$  and  $\sigma^-$  beams are present. Note that the red signal is the signal from figure 2.2.

## Chapter 3

# A Systematic Observation of Zeeman EIT: Results and Discussion

In chapter 2 we described a new optical diagnostic tool we used this summer to ensure adequate polarization purity and alignment of optical and magnetic field axes for clean measurements of EIT. Recall that our Zeeman EIT measurements are performed using a single linearly polarized laser beam and a co-aligned magnetic field. In this chapter we present systematic measurements of EIT both as a function of laser intensity at nearly zero transverse magnetic field, and as a function of transverse magnetic field (i.e. transverse to the co-aligned magnetic field already present) at fixed laser intensity. In both cases, the y-variable plotted is the laser intensity transmitted thru the vapor cell. EIT manifests as a narrow spectral feature centered at zero magnetic field. We perform a systematic study of the linewidth and the amplitude of the EIT signal.

### 3.1 Zeeman EIT Measurements as a Function of Scanning Longitudinal Magnetic Field

Figures 3.1-3.3 are examples of EIT features measured for the  $^{85}\text{Rb } F_g=2 \rightarrow F_e=1,2,3$  transition. These figures show the beam transmission intensity recorded as a function of the longitudinal scanning magnetic field obtained by ramping the solenoid current, as described in Section 2.1.

Figure 3.1 shows the EIT signal obtained for two different values of the transverse magnetic field (applied transversely to the solenoid axis, along the same axis as incident laser polarization, let's call this the y-direction), but at the same low (significantly lower than the saturation intensity) laser intensity of  $0.42 \text{ mW/cm}^2$ . A transverse field of 1 G was found to broaden the linewidth by almost 4X. We found that applying a transverse  $B$ -field in the orthogonal direction, i.e.,  $x$ , merely caused the EIT feature to weaken and disappear.

Figure 3.2 shows the EIT signal obtained for two different values of the laser intensity, but at the same transverse magnetic field of nearly zero. Increasing the laser intensity by ~factor

5X from  $0.42 \text{ mW/cm}^2$  to  $2.1 \text{ mW/cm}^2$  caused the linewidth to increase by a factor of  $\sim 3$ . Notice that the narrowest signal, 99 kHz (FWHM), appears for the case of low laser intensity and low transverse magnetic field.

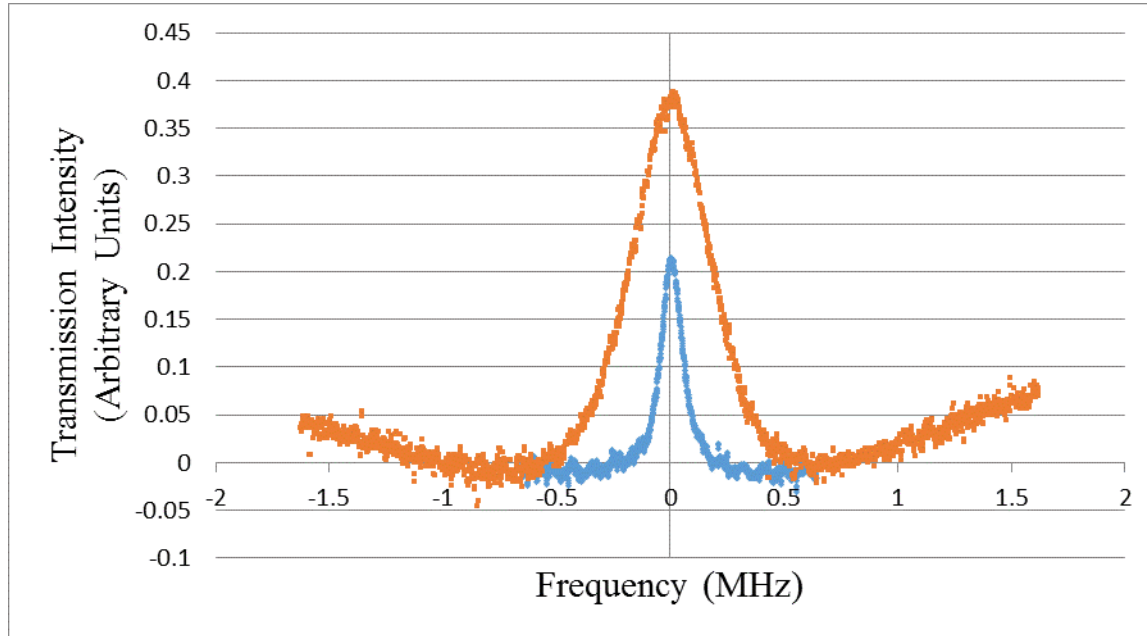


Figure 3.1: Figure 3.1:  $^{85}\text{Rb}$  EIT  $F_g=2 \rightarrow F_e=1,2,3$  transition. For both curves the laser intensity is  $0.42 \text{ mW/cm}^2$ . For the blue curve the transverse magnetic field is nearly zero ( $< 7 \text{ mG}$ ) and the linewidth is measured to be 99 kHz. For the orange curve the transverse magnetic field is 1G, and the measured linewidth is 381 kHz, almost 4X broader.

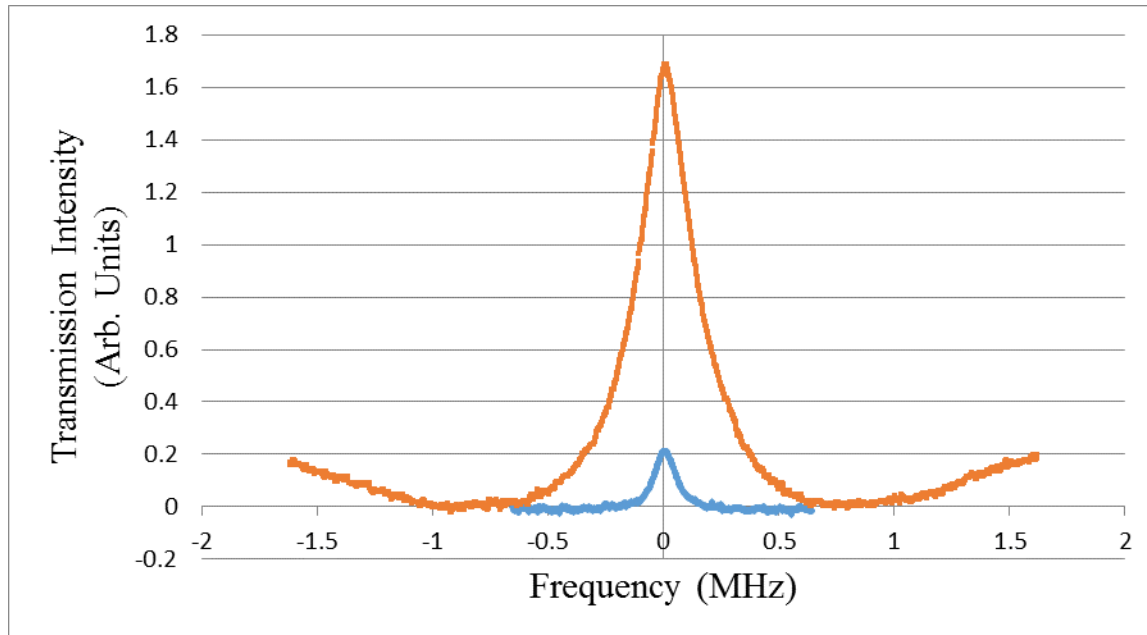


Figure 3.2:  $^{85}\text{Rb}$  EIT  $F_g=2 \rightarrow F_e=1,2,3$  transition. For both curves the transverse magnetic field is nearly zero ( $< 7 \text{ mG}$ ). For the blue curve the laser intensity is  $0.42 \text{ mW/cm}^2$  and the measured linewidth is 99 kHz. For the orange curve the laser intensity is  $2.1 \text{ mW/cm}^2$ , and the measured linewidth is 270 kHz, almost 3X broader.

### 3.2 Dependence of $^{85}\text{Rb}$ and $^{87}\text{Rb}$ EIT Linewidth and Signal-amplitude on Laser Intensity at Zero Transverse Magnetic Field

The first natural “knob” to turn in a systematic characterization of EIT is to study its dependence on laser intensity. A good test of the optical diagnostic discussed in Chapter 2 is to plot the dependence of the EIT feature obtained with the improved setup in Fig. 2.3 and compare this plot with that obtained using the initial setup in Fig. 2.1.

In this Section we took multiple measurements such as in Fig. 3.2 at multiple laser intensities and zero transverse magnetic field, and measured the dependence on laser intensity of the FWHM linewidth and peak size of the EIT feature. The results are plotted in Figs. 3.3 and 3.4 below.

In Fig. 3.3 we plot as a function of laser intensity the linewidth of the EIT feature obtained for the  $^{87}\text{Rb}$   $F_g=1 \rightarrow F_e=0,1,2$  transitions after the improvements discussed in Chapter 2 were made (blue dots) and compared our data with previous data obtained by Jason Barkeloo (MS 2012) [11] on the initial setup in Fig. 2.1. (orange triangles). Clearly, our improved signals are significantly narrower.

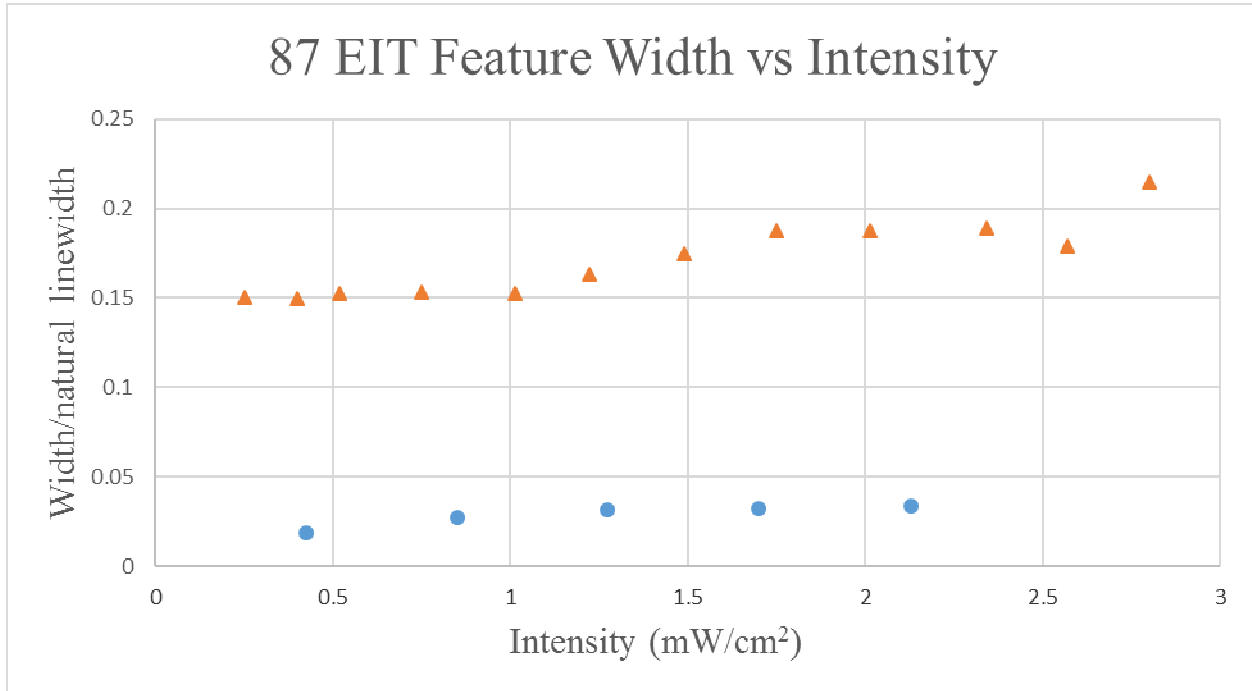


Figure 3.3: Width of EIT feature as a function of Beam Intensity, found in  $^{87}\text{Rb}$   $F_g=1 \rightarrow F_e=0,1,2$  transitions. Data taken with the setup in Fig. 2.1 prior to the improvements in Chapter 2 are shown by red triangles, and the data taken with the improved setup in Fig. 2.3 is shown by blue dots. Note that Width is expressed as a function of the Natural linewidth (6MHz for Rb). Transverse magnetic field is set to 0 G. The EIT linewidths measured by the improved setup are consistently a factor  $>7X$  narrower

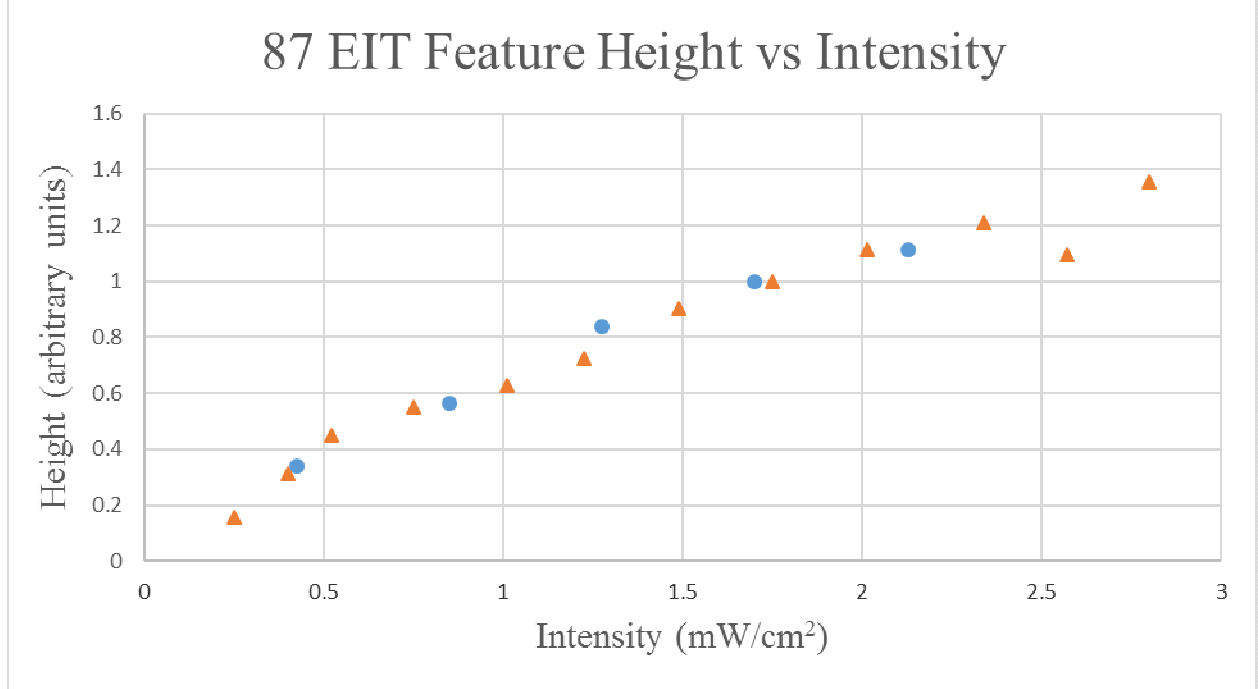


Figure 3.4: Peak Height of EIT feature as a function of Beam Intensity, found in  $^{87}\text{Rb}$   $F_g=1 \rightarrow F_e=0,1,2$  transitions. Data taken with the setup in Fig. 2.1 prior to the improvements in Chapter 2 are shown by red triangles, and the data taken with the improved setup in Fig. 2.3 is shown by blue dots. Transverse magnetic field is set to 0 G. The two data sets are practically identical.

In Fig. 3.4 we plot as a function of laser intensity the height of the EIT feature obtained for the  $^{87}\text{Rb}$   $F_g=1 \rightarrow F_e=0,1,2$  transitions after the improvements discussed in Chapter 2 were made (blue dots) and compared our data with previous data obtained by Jason Barkeloo (MS 2012) [11] on the initial setup in Fig. 2.1 (orange triangles). The two data sets are practically identical.

The finding above is corroborated by further measurements of EIT in  $^{85}\text{Rb}$ , shown below. Fig. 3.5 shows, plotted as a function of laser intensity, the linewidth of the EIT feature obtained for the  $^{85}\text{Rb}$   $F_g=2 \rightarrow F_e=1,2,3$  transitions after the improvements discussed in Chapter 2 were made (blue dots). Our data is again compared with previous data obtained by Jason Barkeloo (MS 2012) [11] on the initial setup in Fig. 2.1. (orange triangles). Just as the above case of  $^{87}\text{Rb}$ , we find that in  $^{85}\text{Rb}$  as well, our linewidths obtained with the improved setup are significantly narrower.

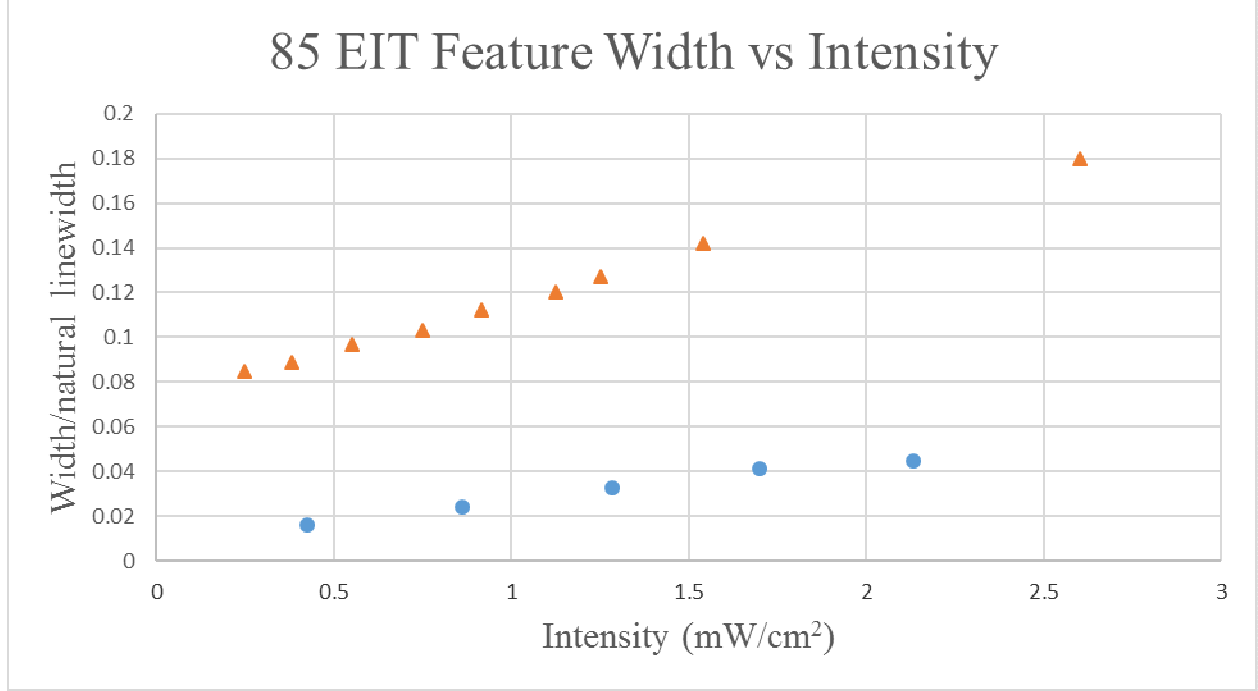


Figure 3.5: Width of EIT feature as a function of Beam Intensity, found in  $^{85}\text{Rb}$   $F_g=2 \rightarrow F_e=1,2,3$  transitions. Data taken with the setup in Fig. 2.1 prior to the improvements in Chapter 2 are shown by red triangles, and the data taken with the improved setup in Fig. 2.3 is shown by blue dots. Note that Width is expressed as a function of the Natural linewidth (6MHz for Rb). Transverse magnetic field is set to 0 G. The EIT linewidths measured by the improved setup are consistently a factor 3-5X narrower.

In Fig. 3.6 we plot as a function of laser intensity the height of the EIT feature obtained for the  $^{85}\text{Rb}$   $F_g=2 \rightarrow F_e=1,2,3$  transitions after the improvements discussed in Chapter 2 were made (blue dots) and compared our data with previous data obtained by Jason Barkeloo (MS 2012) [11] on the initial setup in Fig. 2.1 (orange triangles). Again, just as in  $^{87}\text{Rb}$ , the two data sets for  $^{85}\text{Rb}$  are practically identical.

The results in Figs. 3.3 – 3.4 and 3.5 – 3.6 suggest that our improvements to the setup have succeeded in producing EIT features similar in strength to those obtained with the previous setup, yet significantly narrower. This strongly suggests that the optical diagnostic employed in Chapter 2 is useful. The reduction achieved of the spurious signal in Fig. 2.4 is indeed a consequence of noise suppression and superior alignment, certainly not misalignment.



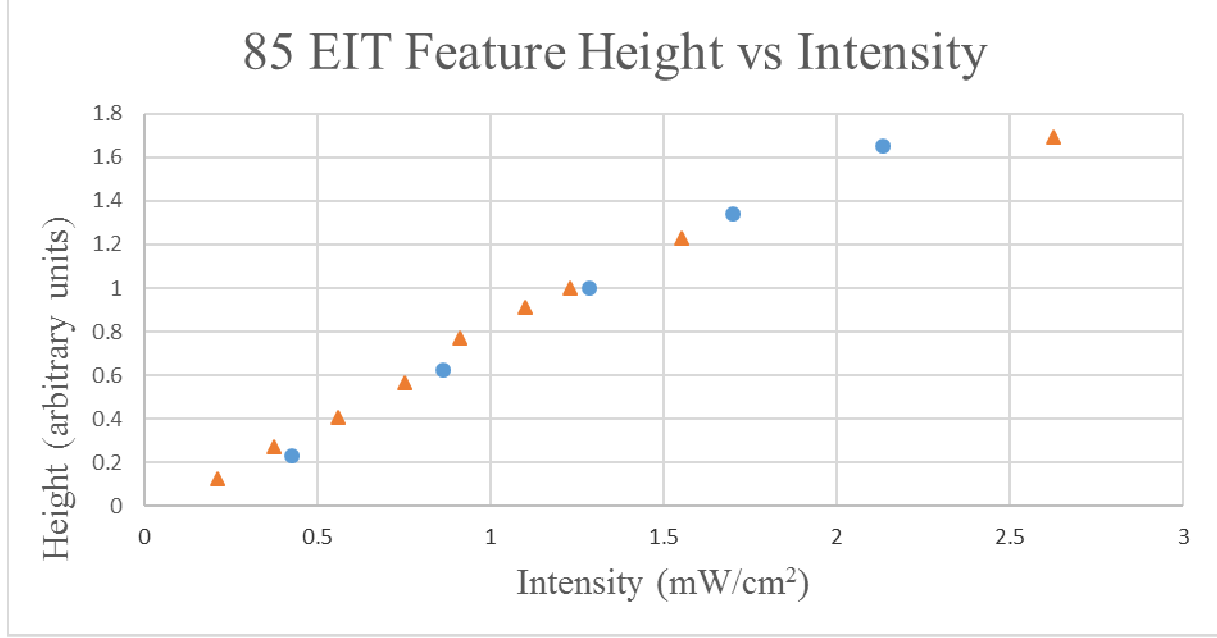


Figure 3.6: Peak Height of EIT feature as a function of Beam Intensity, found in  $^{85}\text{Rb}$   $F_g=2 \rightarrow F_e=1,2,3$  transitions. Data taken with the setup in Fig. 2.1 prior to the improvements in Chapter 2 are shown by red triangles, and the data taken with the improved setup in Fig. 2.3 is shown by blue dots. Transverse magnetic field is set to 0 G. The two data sets are practically identical.

### 3.3 Dependence of $^{85}\text{Rb}$ and $^{87}\text{Rb}$ EIT Linewidth and Signal-amplitude on Transverse Magnetic Field at fixed Laser Intensity

Besides the laser intensity a second “knob” of interest is the transverse magnetic field. In this Section we took multiple measurements such as in Fig. 3.1 at many different values of the transverse magnetic field (pointing along the axis of laser polarization), and measured the dependence on transverse  $\mathbf{B}$  of the FWHM linewidth and peak size of the EIT feature. The results are plotted in Figs. 3.5 and 3.8 below.

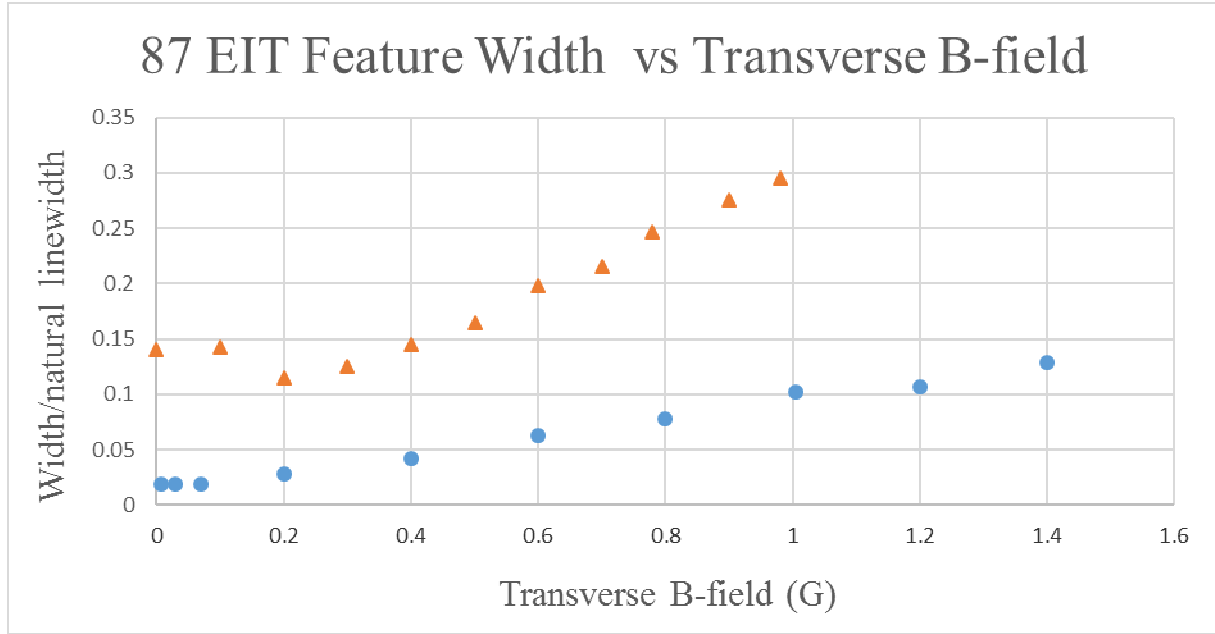


Figure 3.7: Width of EIT feature as a function of transverse magnetic field, found in  $^{87}\text{Rb } F_g=1 \rightarrow F_e=0,1,2$  transitions. Data taken with initial setup (Red triangle) and improved setup (Blue dot) Note that Width is in terms of the Natural linewidth. Beam intensity  $0.42\text{mW/cm}^2$

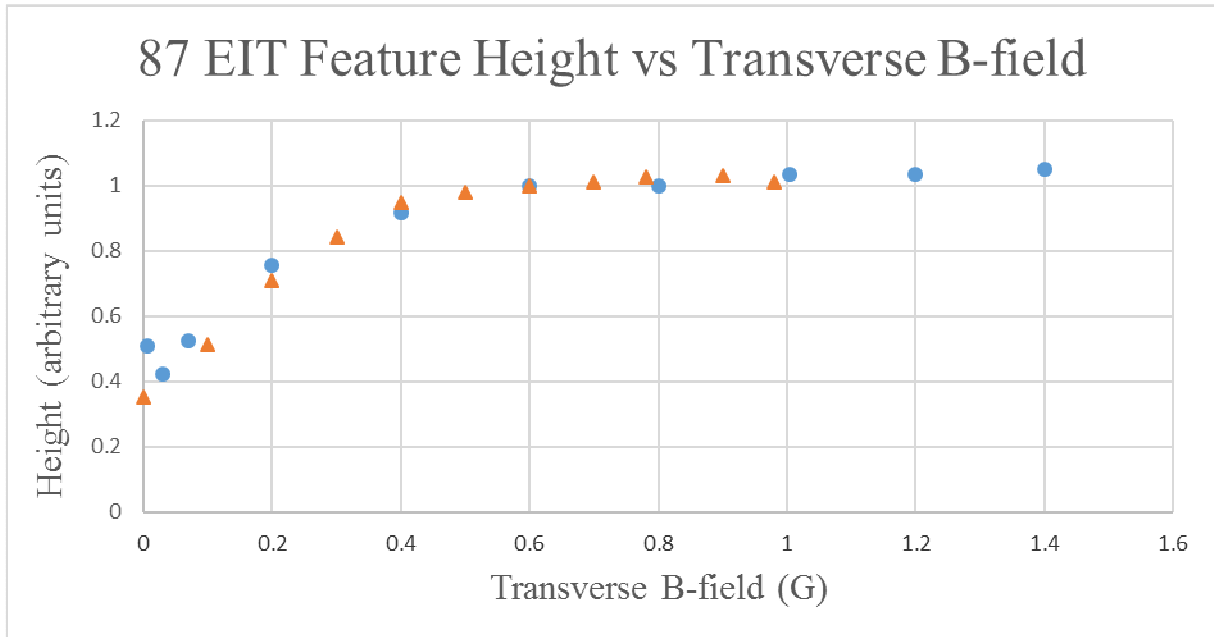


Figure 3.8: Peak Height of EIT feature as a function of transverse magnetic field, found in  $^{87}\text{Rb } F_g=1 \rightarrow F_e=0,1,2$  transitions. Data taken with initial setup (Red triangle) and improved setup (Blue dot). Beam intensity  $0.42\text{mW/cm}^2$

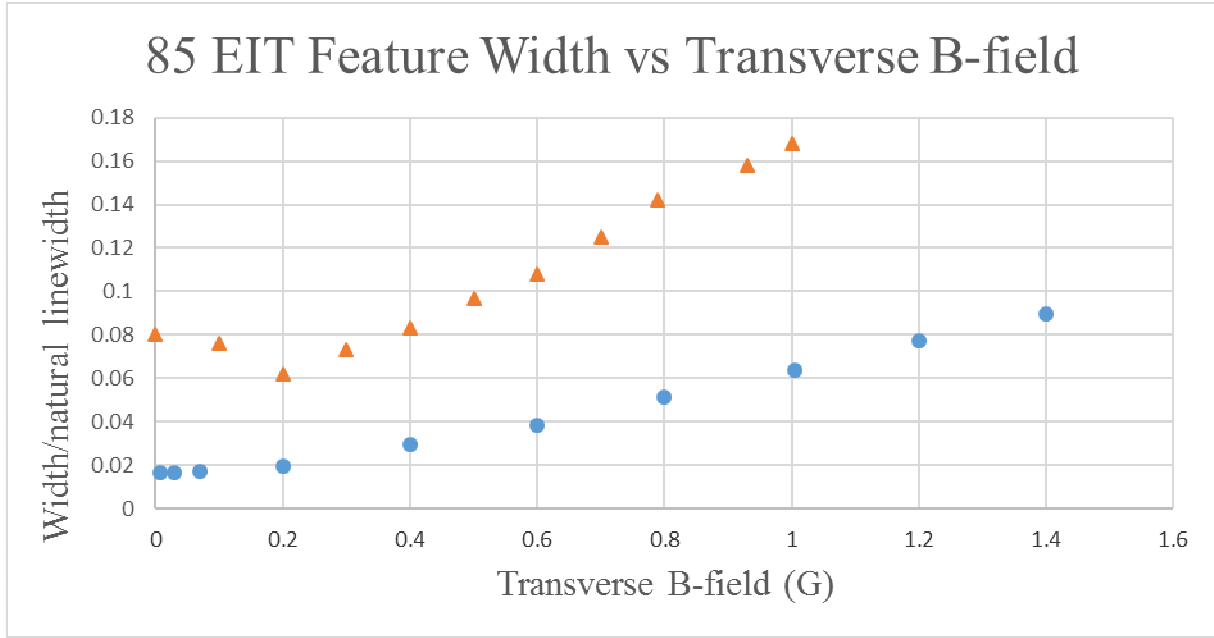


Figure 3.9: Width of EIT feature as a function of transverse magnetic field, found in  $^{85}\text{Rb } F_g=2 \rightarrow F_e=1,2,3$  transitions. Data taken with initial setup (Red triangle) and improved setup (Blue dot) Note that Width is in terms of the Natural linewidth. Beam intensity  $0.42\text{mW/cm}^2$

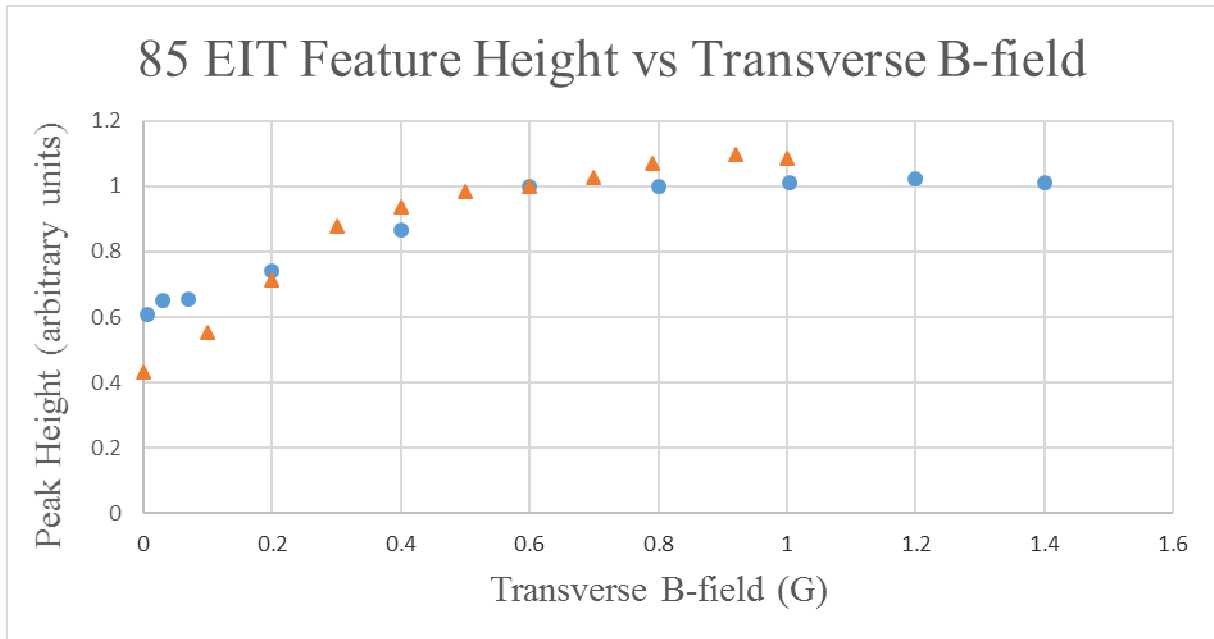


Figure 3.10: Peak height of EIT feature as a function of transverse magnetic field found in  $^{85}\text{Rb } F_g=2 \rightarrow F_e=1,2,3$  transitions. Data taken with initial setup (Red triangle) and improved setup (Blue dot). Beam intensity  $0.42\text{mW/cm}^2$

It is abundantly clear from the data that we have managed to narrow the width of the EIT signal without compromising peak height. In fact the width for  $^{85}\text{EIT}$  transitions became 4 times narrower and nearly 6 times narrower for  $^{87}\text{EIT}$  transitions. It is also important to note that the strange increase in width at near zero magnetic field of the initial setup is now gone. This suggests that stray magnetic fields were present but have now been removed. With the improved setup we will now look into EIT with two circular polarizations.

## Chapter 4

### Future Outlook and Progress towards Slow Light

Interesting possibilities abound in the immediate future owing to the cleaning up of our EIT signals. The plan over the next year follows two main axes of interest:

- a) The groundwork has been set for an investigation into the phenomenon of “Sign Reversal”<sup>12</sup>, where under certain conditions one may smoothly switch between EIT and EIA in a medium simply by varying the relative intensities of the  $\sigma^+$  and  $\sigma^-$  laser beams in Fig. 1.2. Sign reversal is currently of great fundamental interest within the EIT community [12,13].
- b) With some modifications that are well within our capabilities, we can initiate an investigation into the creation of slow light in our apparatus. As mentioned in Section 1.1, this may lead to various exciting applications in the field of quantum information processing [1,5,6,7,18].

In Section 4.1 – 4.3 below we describe the current issues we face with our studies of sign reversal between EIT and EIA. In Sections 4.4 – 4.5 we describe the experimental progress we have achieved toward the production of slow light in our lab.

#### 4.1 Sign Reversal between EIT and EIA

Sign reversal between EIT and EIA, where the experimenter can smoothly transition between EIT and EIA spectral features on a given transition simply by varying the relative intensity of the  $\sigma^+$  and  $\sigma^-$  laser beams in Fig. 1.2, can be simply explained by considering the atomic system in figure 4.1. Here a strong “coupling field” ( $\sigma^+$ ) is pumping the atom from the left most magnetic sublevel to the the right most magnetic sublevel. A weak “probe beam” ( $\sigma^-$ ) is also being applied and is pumping the atoms to the left but less efficiently than the coupling beam which is significantly stronger. The atom spends most of its time in the right most  $\Lambda$  system where the coupling beam simply drives the  $m_{Fg}=0 \rightarrow m_{Fe}=1$  transition until the population has spontaneously emitted to either the  $m_{Fg}=1$  or  $m_{Fg}=2$  states. Due to the presence of the probe

beam the ground states  $m_{Fg}=0$  and  $m_{Fg}=2$  are in superposition. This means the coupling beam has access to atoms in both the  $m_{Fg}=0$  and  $m_{Fg}=2$  states. The probe has a small chance of stimulating the transition from  $m_{Fe}=1 \rightarrow m_{Fg}=2$ . So in essence a coupling photon is absorbed which is then emitted into the probe field. This appears as EIT in the probe since it now has an “extra” identical photon. If the coupling intensity is reduced below the intensity of the probe then a probe photon will be absorbed and then emitted into the coupling beam. This appears as an EIA in the probe beam. Sign reversal of EIT into EIA can be achieved by simply sweeping the coupling beam intensity around the probe intensity.

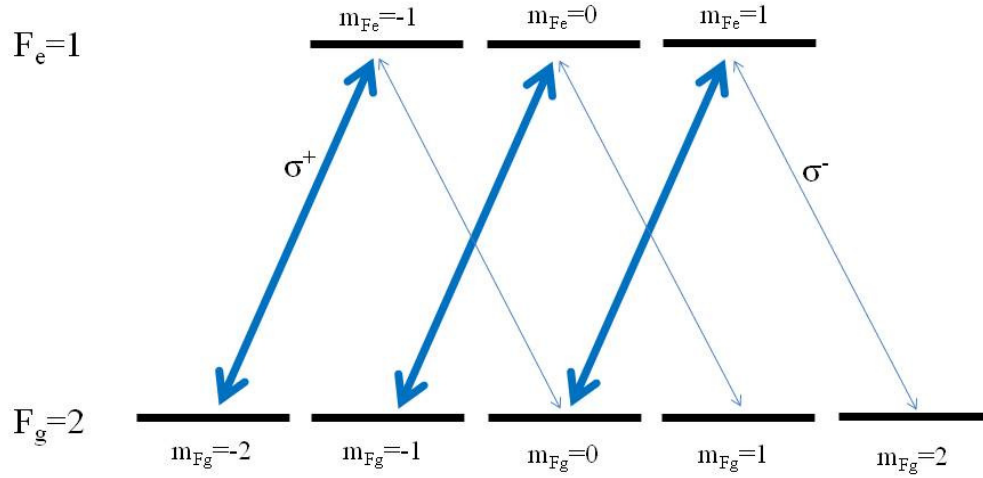


Figure 4.1: Illustration of coupling (strong  $\sigma^+$ ) and probe (weak  $\sigma^-$ ) EIT with orthogonal circular polarizations.

Sign reversal has been performed for atoms in an atomic beam not a vapor cell [Dahl, et al [13], Zigdon *et al* [14],[15] A clear demonstration of sign reversal by varying the relative intensity of a pair of  $\sigma^+$  and  $\sigma^-$  laser beams in a simpler vapor cell setup is of obvious interest. Clearly, this is not possible in our current geometry with the  $\sigma^+$  and  $\sigma^-$  beams arising from a single linearly polarized beam.

Therefore, we decided to adapt our setup in Fig. 2.3 and create two independent orthogonal circularly polarized beams from a single laser beam, so that we can freely alter their relative intensities without the need for phase locking two separate lasers. This adaptation is shown in Fig. 4.2. The only change really is the introduction of a Glan Thompson polarizing beamsplitter (GTBS) to split the single linearly polarized beam into two beams of orthogonal linear polarization (blue and red beams, as shown in Fig. 4.2). The “blue” beam strikes a mirror M (picking up some polarization impurity), hence needs to be cleaned by passing through a Glan

Thomson polarizer GT before being recombined at a 50:50 nonpolarizing beamsplitter BS with its orthogonally polarized “red” partner beam that had passed straight through the GTBS. The recombined blue and red beams, of orthogonal linear polarization with respect to each other, pass together (now depicted as a purple beam) through a quarter waveplate QWP which prepares them as two co-propagating beams (one is the “coupling”, the other the “probe”) of orthogonal *circular* polarizations. These two beams are very slightly misaligned with respect to each other so that just one of these beams is actually observed on a photodiode PD after passing through the vapor cell. Just as in the observation of EIT in Chapter 2, the transmission spectrum of one of the beams is observed as a function of scanning longitudinal magnetic field, for many different values of the intensity of the other beam.

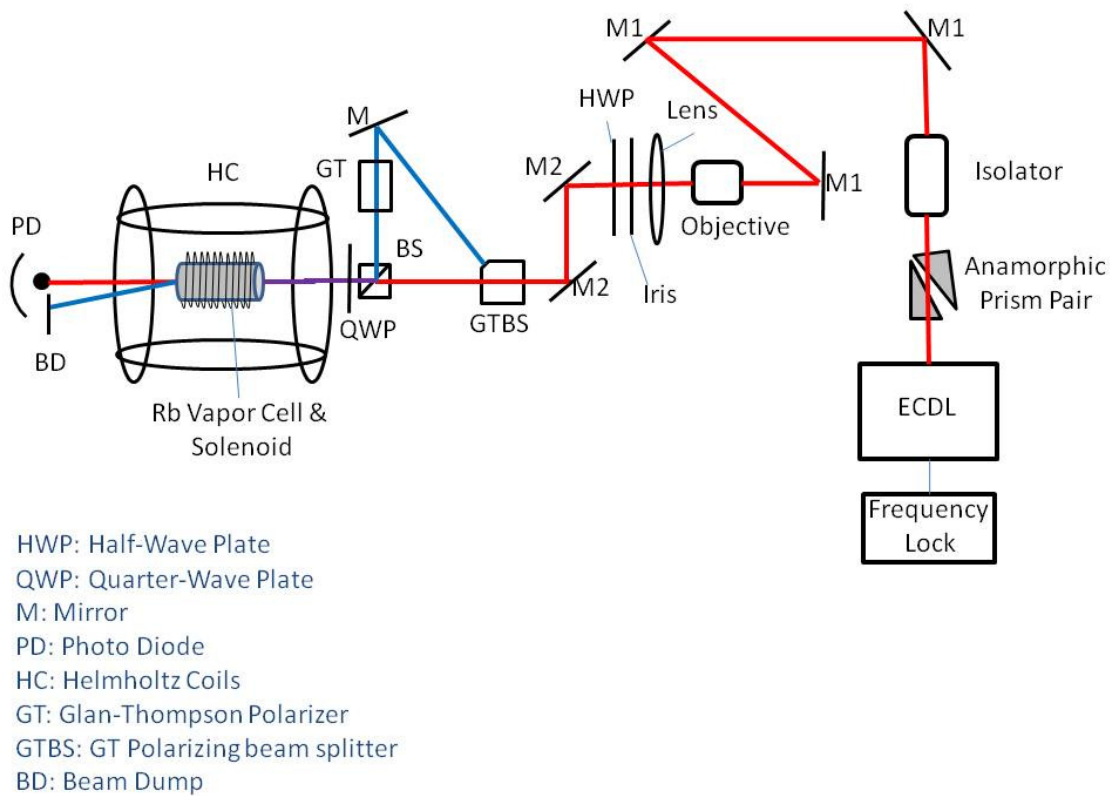


Figure 4.2: Setup for EIT with circular polarized light. Note that quarter waveplate is set such that the coupling beam (blue) and probe beam (red) are orthogonal and circular polarized. Only the probe beam is viewed.

## 4.2 Preliminary Results

A preliminary measurement of the probe transmission spectrum is shown in figure 4.3. It is difficult to say where to measure the full width at half maximum since there is such a large difference between the bottom of the left side of the “hump” and the right side. Taking the FWHM using the left side as the base of the “hump” a width of about 650kHz is measured. Although this is still sub natural linewidth it seems unlikely that this is a genuine EIT signal. Since we succeeded with the single linearly polarized beam in Chapter 2 there is no reason why we should not succeed with two independent circularly polarized beams. However, we ran out of time to investigate this further investigation. In the future a possible simplification to this experiment can be made by working in a “cleaner” set of transitions such as the D1 lines of  $^{87}\text{Rb}$  where the excited state splitting exceeds the Doppler linewidth.

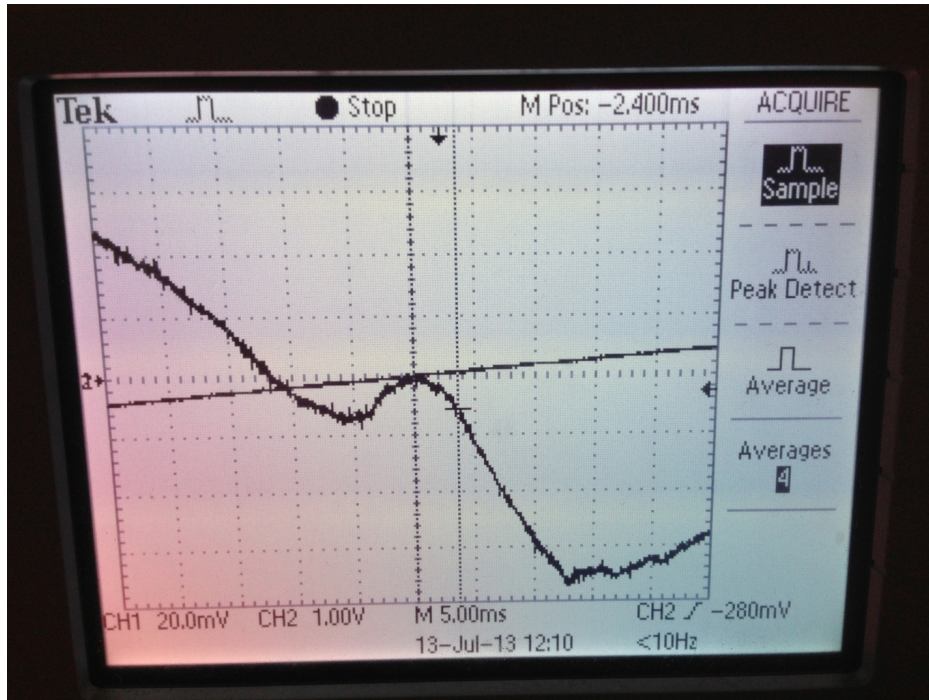


Figure 4.3: Signal observed with 2 orthogonal circular polarized beams when viewing the probe. FWHM of the bump is ~650kHz

## 4.3 Introduction to Slow Light

Slow light refers to the situation where the group velocity  $v_g$  of a light pulse in a medium is a millionfold less than  $c$ , the speed of light in vacuum. Consider a plane wave of angular



frequency  $\omega$  and angular wave number  $k$ , propagating through a medium of refractive index  $n$ , mathematically described by

$$E(z, t) = Ae^{i(kz - \omega t)}$$

where the phase of the wave can be written as:

$$\phi = \frac{n\omega z}{c} - \omega t$$

For the pulse to propagate without distortion we set  $\phi$  constant to the first order:

$$\frac{d\phi}{d\omega} = 0 = \frac{dn}{d\omega} \frac{\omega z}{c} + \frac{nz}{c} - t$$

Using  $z = v_g t$  we obtain

$$v_g = \frac{c}{\left(n + \omega \frac{dn}{d\omega}\right)} = \frac{d\omega}{dk} \rightarrow n_g = n + \omega \frac{dn}{d\omega}$$

Defining  $n + \omega \frac{dn}{d\omega}$  as the group refractive index  $n_g$  it can be readily seen that an increase in  $n_g$  will result in a slower group velocity. A large  $n_g$  can be induced in an EIT setup where the dispersion  $dn/d\omega$  is inherently large. That is to say the change in absorption of the EIT signal happens within a small frequency window ( $\sim 100$  kHz), Figure 4.4. This sudden change in refractive index leads to slower group velocities.

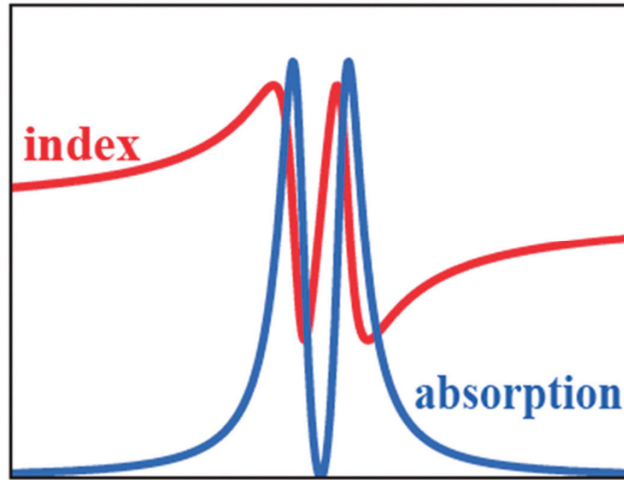


Figure 4.4 displays both the index of refraction (red) and the absorption spectrum of EIT (blue) as a function of frequency. Notice the rapid change in the refractive index within the EIT window. Reproduced from [16]

#### 4.4 Experimental Issues and Progress achieved

Our setup is almost adequate to initiate the experimentation in slow light but the following significant modifications need to be made. Progress achieved to date on these modifications is described.

##### 4.4.1 New Laser Diode for tuning to the D1 Transitions of Rubidium

A new laser diode capable of exciting the D1 transitions at 795nm has been recently purchased. The D1 transitions are the relevant hyperfine transitions for the study of slow light since their separation exceeds the Doppler width. This avoids the problem in the D2 lines of needless joint excitation of multiple hyperfine transitions that overlap owing to their separation being less than the Doppler width. Outfitted with this new diode we plan to investigate EIT and sign reversal with linear and circular polarizations, and pave the way for the future pursuit of slow light.

Measured with a spectrometer, the center wavelength of the laser diode at room temperature is at 788nm. As discussed in Appendix 1 the home built ECDL is capable of tuning a laser diode  $\pm 5$ nm from the center wavelength. To stretch the wavelength further one needs to also tune with temperature. Figure 4.4 shows how a single mode laser diode's wavelength changes with temperature.

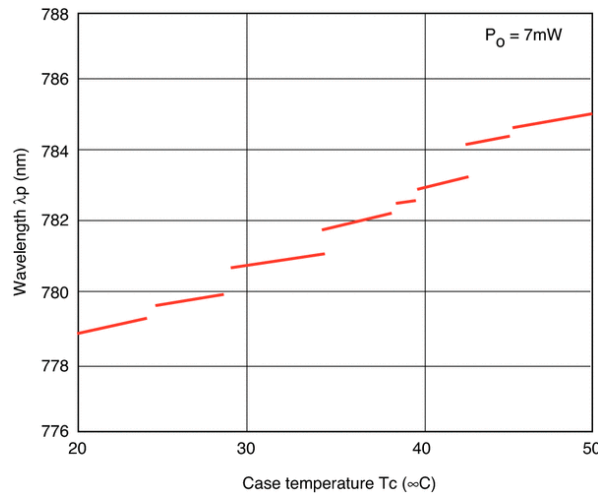


Figure 4.5: Wavelength dependence on temperature of laser diode. Reproduced from [17]

To find resonance in the vapor cell a combination of detuning via diffraction grating and temperature was used. We increased the temperature by  $.1^\circ\text{C}$  then swept the wavelength via

diffraction grating. At 30°C a wavelength of 796.41nm was observed. At this point I varied the current while sweeping the diffraction grating around 795nm until resonance with the D1 lines was found. At 796nm and current value of 105mA, resonance in the vapor cell was observed. This suggests that the spectrometer needs to be calibrated.

The next step is to find the saturated absorption spectrum as described in Appendix 1. Unfortunately it was discovered that although the screws holding the diode in place were tight the diode was free to move around. At closer inspection it was decided that to fix this problem deeper screw holes need to be made such that the screw head can press fully against the back diode, keeping the diode securely locked in place. Due to time constraints this was not possible for me to pursue. Once this issue is resolved the saturated absorption spectrum can be found. Because there are only two excited states in the D1 transitions for both  $^{85}\text{Rb}$  and  $^{87}\text{Rb}$  the spectra will look significantly simpler than their D2 counterparts. As shown in figure 4.5 there will be four spectra, consisting of two transition peaks and one crossover peak.

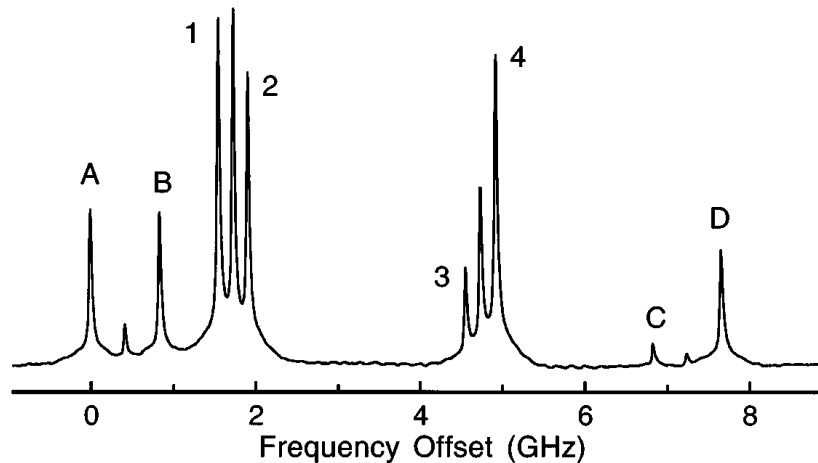


Figure 4.6: SAS spectrum for the D1 transitions The lettered peaks are the  $^{87}\text{Rb}$  transitions and the numbered peaks are  $^{85}\text{Rb}$  transitions. Unlabeled peaks are crossover peaks. Reproduced from [18]

#### 4.4.2 Oven for Heating Vapor Cell to Increase EIT Signal

At room temperature rubidium exists as both solid and gas within the vapor cell. As the temperature decreases, the rubidium vapor will condense on the cell walls. Even at room temperature condensed rubidium is visible on walls of the vapor cell. By heating the cell more vapor will be available for the light to interact with, thus enhancing the signal strength of EIT. Figure 4.6 shows a plot of vapor density as a function of cell temperature.

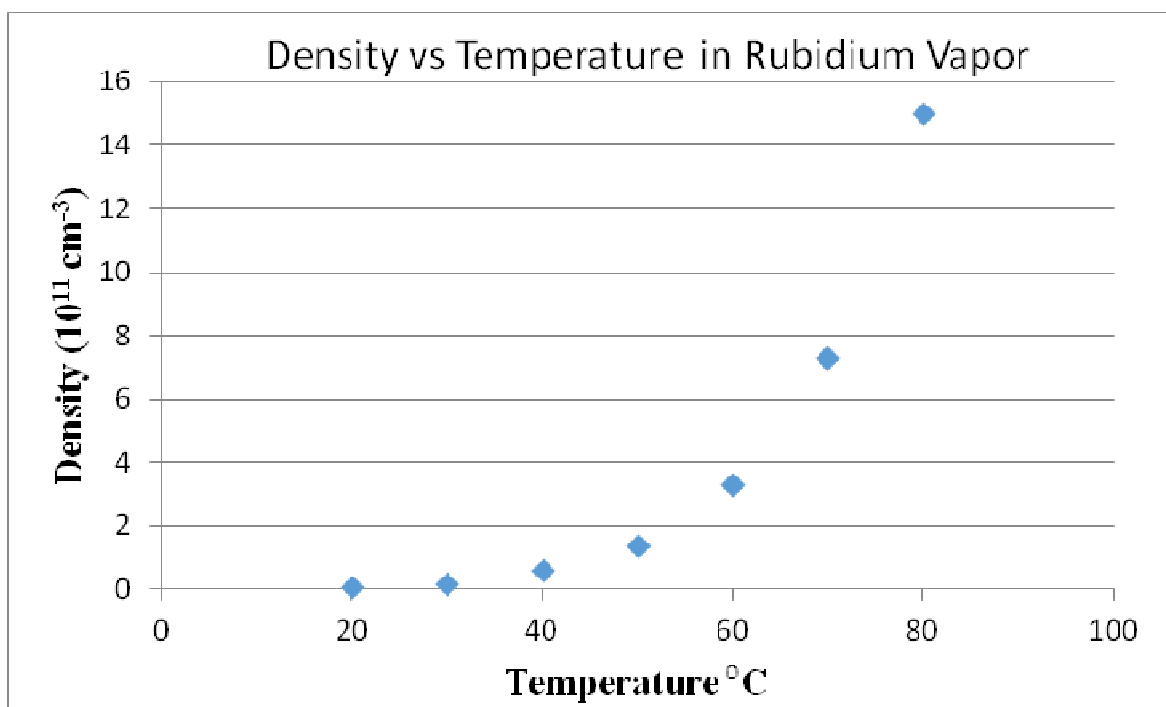


Figure 4.7: Plot of the density of rubidium within the temperature regime we are studying. Data from [19]

As this is a magnetically sensitive apparatus using any resistive heating within the range of the Helmholtz coils will interfere with EIT resonance. We have circumvented this issue by channeling the heat from a standard room heater, placed well outside the EIT setup, into a PVC pipe chamber which houses the vapor cell. An Arduino micro controller reads the temperature from a thermocouple. When the temperature reaches a set value the Arduino outputs a digital signal to the relay. When the relay receives digital 'high' the heater is on, and when the relay receives digital 'low' the heater is off. A fan pushes the hot air near the heater through flex pipe. We have been able to keep the cell at  $60 \pm 5^\circ\text{C}$  using this method. The construction of the circuit and Arduino code can be found in Appendix 1.

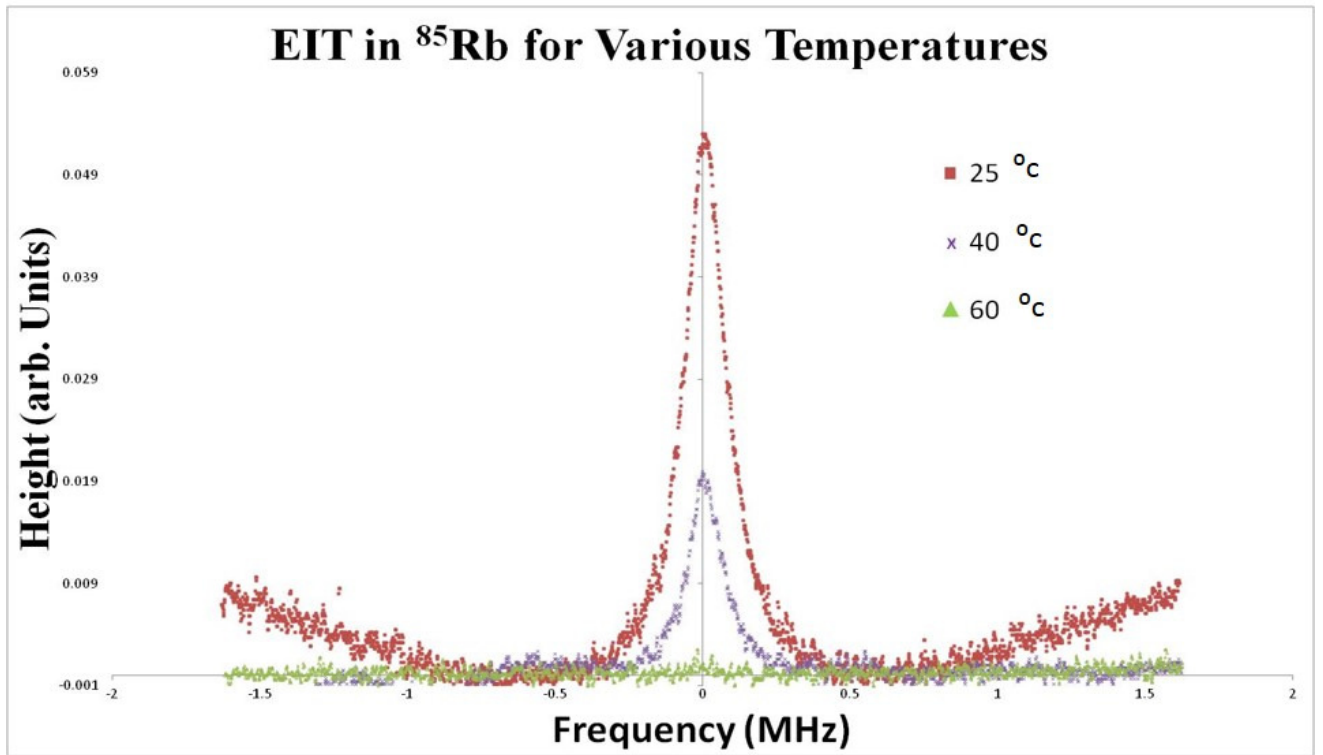


Figure 4.8: Observed EIT signals for  $^{85}\text{Rb}$  at room temperature,  $40^\circ\text{C}$ , and  $60^\circ\text{C}$

We have tested our oven setup by measuring EIT in  $^{85}\text{Rb}$  at three different temperatures, room temperature,  $40^\circ\text{C}$ , and  $60^\circ\text{C}$ . What we found is quite surprising. The signal actually decreased with temperature (figure 4.7) despite there being more rubidium atoms for the light to interact with. We have a couple untested suspicions as to why this would happen. First, it is possible that there was too much uneven heating of the cell

which could cause the vapor to condense on a cool spot of the glass. This would mean that we are actually decreasing the amount of rubidium vapor in the cell. Second, it could be that the amount of time the atoms spend in the cross-sectional area of the beam and the increased amount of collisions between atoms disrupted the EIT process.

#### 4.4.3 Creation of Pulsed Light for Demonstration of Slowing of Light Pulses

We will need to adapt our setup such that the incident light is pulsed, so that we can observe the slowing of the light pulses. To create these pulses a split beam, dual acoustic-optic modulator (AOM) setup, shown in figure 4.8, will be implemented. The purpose of this dual AOM setup is to create two pulses – the signal pulse and the control pulse. The signal and control pulses pass through the vapor cell. The reference pulse does not pass through the vapor cell but travels over an identical path length, thus providing a  $t=0$  reference for measuring the slowing of the signal.

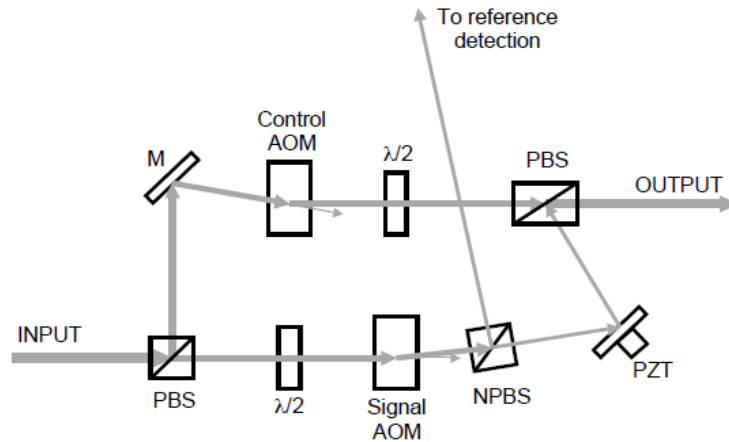


Figure 4.9: Dual AOM setup, used for signal field generation as well as independently regulating the power of the pump and probe fields. (Reproduced from [20])

In this configuration, filtered light from the external cavity diode laser is split at a polarizing beam splitter (PBS) into two orthogonally linear polarized light beams. The vertically polarized light is sent through the control AOM and the horizontally polarized light is first converted by the half wave plate to vertically polarized and then passed through the signal AOM. A reference pulse is created using the non-polarizing beam splitter (NPBS). Both the control and signal fields are recombined by the final PBS. A mirror attached to a piezo-electric transducer (PZT) is placed in the path of the signal

field prior to the output. This is used to vary the path length of the signal field, keeping it in phase with the control field. It is important to note that this AOM setup is also used for varying the laser intensity.

## Part 2

### Optical Sensing

In this part of the thesis I will discuss a new model for measuring the refractive index within highly turbid media, developed by our optical sensing team. I start in Chapter 5 by stating our motivation for optical sensing in highly scattering opaque (also known as “turbid”) media. and describe our setup for collecting data. Next, in Chapter 6 I discuss our new empirical model of total internal reflection (TIR) from highly turbid media and how it differs from traditional Fresnel theory. I provide experimental validation for our model, and apply our sensor and model to biosensing.

### Chapter 5:

#### 5.1 Motivation and Background

Developing an accurate model for finding the refractive index of turbid media, and extending this model toward in-situ particle sizing, has been of great interest to the scientific community and has generated much debate [21, 22, 23, 24, 25,26]. This is because understanding the optical properties of highly turbid media, like biotissue and crude petroleum are of immense interest to the scientific and industrial community. By far the most widely used method for determining the refractive index is based on a determination of the critical angle in total internal reflection (TIR) from the surface of the medium [22]. However the critical angle does not exist for turbid media.

Recently we showed Fresnel theory was being applied erroneously by previous workers [21, 23, 27] and that angle dependent penetration of the incident light into the turbid medium needs to be accounted for [28]. In Ref. [24] we tested our new model of TIR on milk and milk-cream mixtures which cover (from fat-free milk to heavy whipping cream) a wide range of turbidities and are hence convenient. However milk and cream consist of an aqueous colloidal suspension of fat globules with widely ranging particle size and distribution, and are therefore difficult to model in detail. This is a significant drawback because a detailed theory of TIR and refractive index must incorporate the size of the scattering particles.



It is remarkable that despite the realization that particle size plays an important role in TIR, there exists to date no theory or experiment that explicitly investigates this in a satisfactory manner. For instance, Reyes-Coronado et al [25] cite “persistent inconsistencies in their observed TIR signals, causing them to work with the transmitted light instead but in doing so they are restricted to samples of extremely low turbidity. Pena-Gomar et al [29] attempt to systematically investigate the effect of particle size on TIR but are hampered by the extremely poor resolution of their instrumentation (arising from the use of a goniometer for mechanically adjusting the angle of incidence of the laser beam on the sample surface). Furthermore, the works [25] and [29], as well as works [24] and [26], were performed before Ref. [28], and therefore do not include angle dependent penetration of the incident beam into the turbid medium. Hence the theoretical treatments in these works are incomplete.

Below I describe our experimental setup for a novel home-built refractive index sensor that is rugged, compact, inexpensive, and capable of measuring the complex refractive index of highly turbid media in near real-time. We use our sensor to perform a first accurate demonstration of in-situ particle sizing in highly turbid media.

## 5.2: Method and Setup

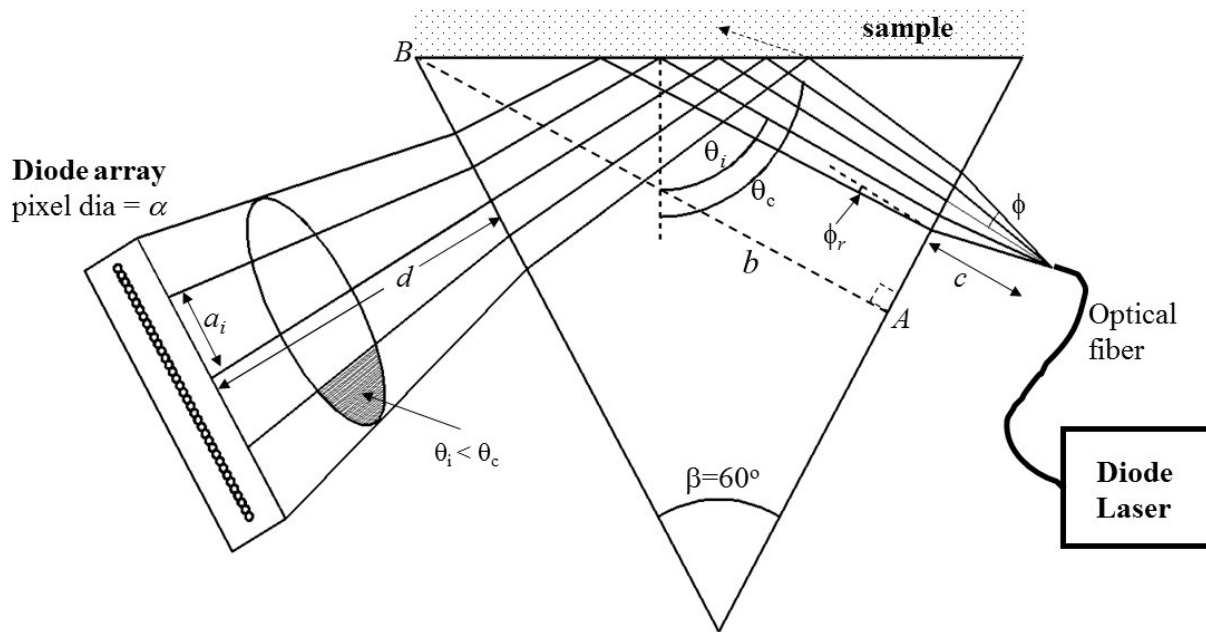


Figure 5.1 Schematic of home built TIR based refractometer.

In figure 5.1 we show our set up for TIR measurement. The sample is placed on top of a glass prism and illuminated by a diode laser of wavelength 660nm connected to a optical fiber. The fiber yields a divergent laser beam, of angular width  $\sim 14^\circ$ , positioned such that the central ray is normal to the prism side. This divergent beam enables us to sensitively study, without mechanical noise, the transition from TIR to non-TIR. This light is reflected from the prism-sample interface on to a one dimensional pixel array (1024 pixels, pixel diameter  $14\mu\text{m}$ ), which measures the intensity of the reflected light. In the case of TIR the pixels will be illuminated while in the case of non-TIR the pixels will be dark. We convert the pixels to angles using

$$\theta_i = \beta + \delta_1 + \tan^{-1}[a_i(b + n_{prism}(c + d)) + \delta_2] \quad (5.1)$$

Here  $\delta_1$  is the error associated with the departure from normal incidence of the central laser ray, and  $\delta_2$  is the error in distance measurements  $c$  and  $d$ , while the remaining symbols in Equation (5.1) are depicted in figure 5.1. If we denote  $I_r$  as the reflected intensity and  $I_i$  as the incident intensity the next step is to measure the  $I_r / I_i$  curve for the sample medium as a function of  $\theta_i$ . To do this we first find  $I_i$  by selecting a prism such that for all angles of incidence we obtain TIR, when air is the sample. Then to find  $I_r$  we place the sample directly on top of the prism and measure the reflected intensity profile. Finally we compute the ratio  $I_r / I_i$ . Note that our setup contains no moving parts hence is at least an order of magnitude higher, if not more, in sensitivity than all previous methods by other workers [30].

### 5.3 Fresnel Theory and the Corrected Angular Model

Here we recount the relevant features of the theory for our new model of TIR developed in [28]. For a basic illustration of TIR see figure 5.2. For transparent media one merely needs to determine the critical angle  $\theta_c$  at which TIR first occurs.

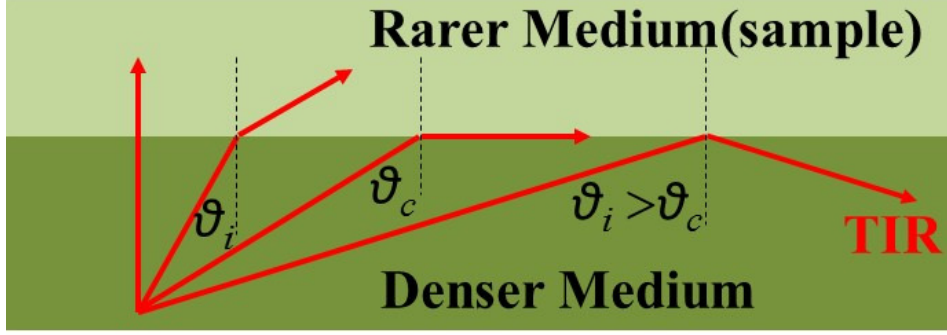


Figure 5.2 TIR occurs when  $\theta_i > \theta_c$

For turbid media the story is quite different. Turbidity refers to multiple scattering undergone by an incident light beam due to suspended colloids within the medium. Turbidity is described by the attenuation coefficient  $\alpha$ , which measures the loss of directed radiation per unit length through the sample due to scattering and/or absorption; i.e., the intensity  $I(z)$  of a light beam propagating in the  $z$  direction through the medium can be written as  $I(z) = I_0 \exp(-\alpha z)$ , where  $I_0$  is the intensity at  $z=0$ . The refractive index becomes complex with the real part  $n_r$  describing the usual bending of light at the interface, and the imaginary part  $n_i$  describing the attenuation undergone by the light. Mathematically  $n_i = c\alpha/2\omega$  where  $c$  is the speed of light in a vacuum, and  $\omega$  is the frequency of the laser light. So the complex refractive index is  $n_{sample} = n_r + in_i$ . Fresnel theory yields for the reflectance profile [23]

$$\frac{I_r}{I_i} = \frac{M + P^2 \cos^2 \theta_i - \sqrt{2} \cos \theta_i (M + \sin^2 \theta_i) \sqrt{M + L}}{M + P^2 \cos^2 \theta_i + \sqrt{2} \cos \theta_i (M + \sin^2 \theta_i) \sqrt{M + L}} \quad (5.2)$$

where we have used  $P = (n_r^2 + n_i^2) / n_{prism}^2$ ,  $L = [(n_r^2 + n_i^2) / n_{prism}^2] - \sin^2 \theta_i$  and

$$M = \sqrt{P^2 - 2L \sin^2 \theta_i - \sin^4 \theta_i}$$

In Ref. [27] we demonstrated the first successful measurement of  $n_r$  and  $n_i$  from the reflectance profile described by equation 5.2. We were successful because we accurately took into account the angle dependent penetration undergone by the incident light during TIR into the sample medium. This penetration gives rise to angle dependent attenuation as well. Traditional Fresnel theory fails to take into account this angle dependent attenuation by erroneously defining  $n_i$  only for light normal to the plane of incidence.

In Ref. [7] we correct this flaw by deriving a new angle dependent expression  $n_i(\theta_i)$ :

$$n_i(\theta) = n_i(4\pi n_{prism} \sqrt{(M - L)/2})^{-1} \quad (5.3)$$

where  $n_i$  is the traditional expression defined at normal incidence, and the term  $4\pi n_{prism} \sqrt{(M - L)/2})^{-1}$  is the angular correction factor. It is this angle dependent  $n_i(\theta_i)$ , not simply  $n_i$ , that needs to be substituted in equation 5.2 in order to extract the correct values for  $n_r$  and  $n_i$  from the data.

#### **5.4 Use of Angular Model to Create Accurate Empirical Model of Total Internal Reflection in Highly Turbid Media**

Recently we published a paper[31] where we demonstrate, to the best of our knowledge, a first accurate empirical model for reflectance measurements from highly turbid media over the full range of incident angles, i.e., for reflectivity values going from unity in the total internal reflection regime to nearly zero when almost all the light is transmitted. Evidence that our model is accurate is provided by extraction of the particle size, followed by independent verification with dynamic light scattering. Our methodology is in direct contrast with the prevalent approach in turbid media of focusing on only the critical angle region, which is just a small subset of the entire reflectance data.

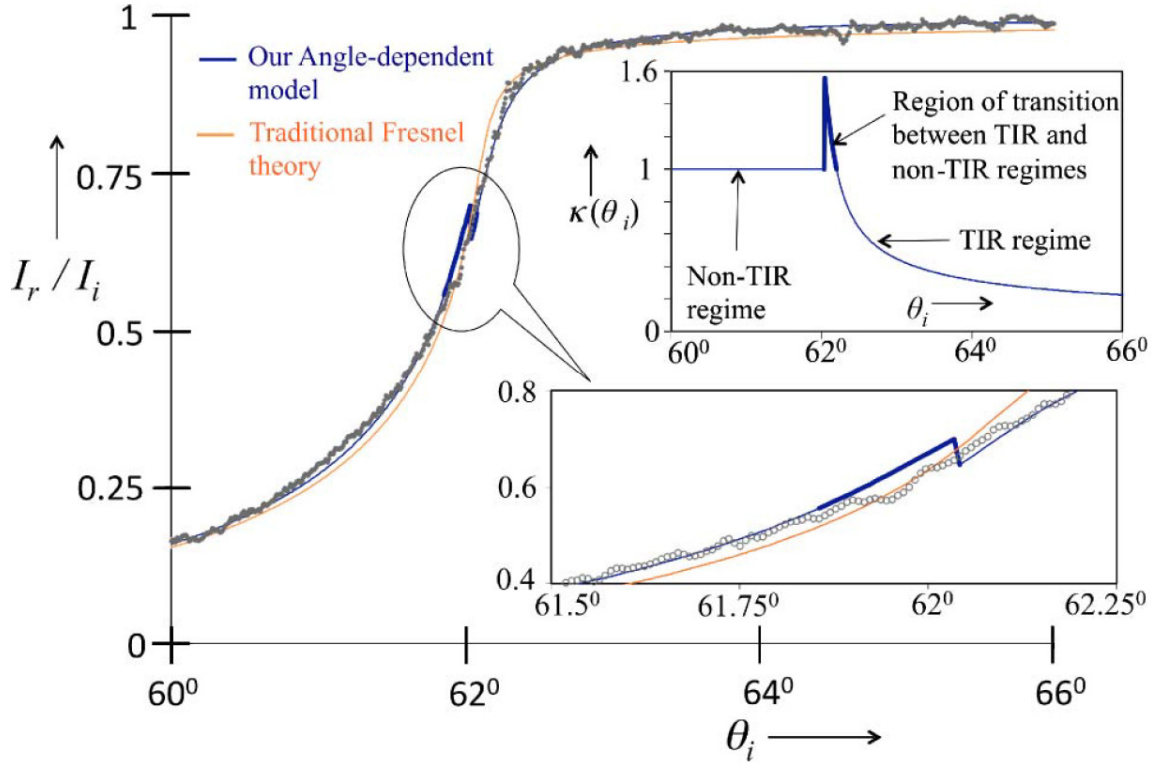


Figure 5.3 Reflectance data (1000 datapoints) for aqueous solution of polystyrene spheres (dia  $0.356 \pm 0.014 \mu\text{m}$ ). Solid lines are theoretical fits; dots are data. Both the angle-dependent model [dark blue; see text for explanation of spike (bold)] and traditional Fresnel theory (light orange) fit data closely, yet only one is correct.

Figure 5.3 shows  $I_r/I_i$  curves as a function of incident angle  $\theta_i$  for a highly turbid aqueous solution of latex microspheres. Each datapoint in the figure is represented by a gray dot, which is an average over 100 measurements. To obtain  $I_i$  we first measure the reflected intensity profile with no sample. Next we find  $I_i$  by measuring the reflected intensity profile with the sample on the prism. Finally the ratio of the two intensities is found and plotted as a function of angle. The prism material and angle is chosen such that TIR occurs over all angles without the sample on the prism and the TIR non-TIR region transition of the sample occurs at some angle within the range of the divergent beam.

The light-orange and dark-blue curves in Fig. 5.3 are best possible fits obtained by traditional Fresnel theory (denoted by F from here on) and by our angle-dependent model [denoted AM] respectively. Each fit is optimized by minimizing its mean-square-deviation (MSD).

This method was repeated for 5 different particle sizes with varying concentrations (table 5.1). Notice that the ratio of MSD values of the AM to F shows that F actually fits the data better

than the AM for particle sizes with a diameter of less than half the wavelength (660nm). So which model should be trusted? We chose to calculate the particle size of the sample, using Mie theory, based on the  $n_r$  and  $n_i$  given by the two models. These particle sizes were then compared to DLS (dynamic light scattering) measurements, the standard technique used for measuring particle size. Table 5.1 shows that although the Fresnel theory had a better fit (b/c the MSD ratio of AM: F in the last column is  $> 1$ ) for the smaller particles (sizes 0.054 to 0.2  $\mu\text{m}$ ) it fails to accurately predict the particle size of the samples. On the other hand, for these same particles, the particle sizes extracted from our AM model are in good agreement with DLS; the discrepancy is less than 10% in all cases. Of course, for the larger particle sizes (0.356 to 0.5  $\mu\text{m}$  in Table 5.1) and turbidities, not only does our AM model fit the data better than F (the MSD ratio of AM: F is  $< 1$ ) but the extracted particle sizes continue to be in good agreement with DLS, even as the particle sizes extracted by the F-model become increasingly erroneous. This implies the  $\alpha$  values extracted by AM are correct as well (as should be the  $n_r$  values, which we do not show for brevity). By contrast, it is only for the sample with the lowest turbidity (and lowest particle size) that particle sizing from F theory (Column 7) has similar agreement with DLS as our AM model. For all other samples, disagreement of F with DLS is significantly large, tending to grow with rising turbidity and/or particle size, exceeding 40% for 0.5  $\mu\text{m}$  particles at  $\alpha = 578 \text{ cm}^{-1}$ . Note that F theory's prediction for  $\alpha$  in this case differs from AM by more than a factor of two.

The reason our model succeeds and traditional Fresnel theory fails is that, while the F-model uses constant  $n_i$  at all angles, our model switches between constant  $n_i$  in the non-TIR regime and angle-dependent  $n_i(\theta)$  in the TIR regime. This switch is clearly shown in the two insets of Figure 5.3 and manifests as a “spike” or discontinuity. This spike results from the fact that in a highly attenuating medium the concept of a critical angle is untenable; hence one really does not know where the TIR regime ends and where the non-TIR regime begins. The upper inset of Figure 5.3 is a plot as a function of angle of the angular correction factor from equation 5.3, here denoted as  $\kappa$ . The transition between the TIR and non-TIR region is ambiguous however the AM approach aims to fit the entire curve,  $\sim 1000$  points, and hence this feature, which occurs over less than 2% of the data, can be “ignored”. Our results were published recently in Ref. [29]. In the next Section we apply this new model to a demonstration of accurate in situ particle sizing in intralipid fat emulsions.

Manu. Size ( $\mu\text{m}$ )	Vol. Frac. (%)	DLS Size ( $\mu\text{m}$ )	$\alpha$ AM ( $\text{cm}^{-1}$ )	$\alpha$ F ( $\text{cm}^{-1}$ )	Size Error AM	Size Error F	MSD Ratio AM/F
0.054	2.48	0.059	4	6	-8%	+7%	1.1
0.1	0.95	0.124	17	30	+2%	+30%	1.0
0.2	2.38	0.185	91	82	-6%	-10%	1.3
0.2	4.76	0.185	223	146	+3%	-14%	1.4
0.2	9.52	0.187	475	247	+5%	-21%	1.2
0.356	2.51	0.385	379	193	+0.5%	-34%	0.6
0.5	0.95	0.477	172	109	-7%	-31%	0.5
0.5	2.86	0.477	578	252	+3%	-42%	0.2

Table 5.1: Comparison of Particle-Sizing by AM and F Models for Different Particle Sizes and Concentrations (Size Errors in Columns 6 and 7 are Calculated Relative to the DLS Sizes in Column 3)

### 5.5: Application of our New Model of TIR to in situ Particle Sizing and Biosensing

Recently we published an accurate measurement of the complex refractive index in an intralipid emulsion, and thereby extracted the average scatterer particle size using standard Mie scattering calculations [32]. Our method is based on measurement and modeling of the reflectance of a divergent laser beam from the sample surface. In the absence of any definitive reference data for the complex refractive index or particle size in highly turbid intralipid emulsions, we base our claim of accuracy on the fact that our work offers several critically important advantages over previously reported attempts. First, our measurements are in situ in the sense that they do not require any sample dilution, thus eliminating dilution errors. Second, our theoretical model does not employ any fitting parameters other than the two quantities we seek to determine, i.e., the real and imaginary parts of the refractive index, thus eliminating ambiguities arising from multiple extraneous fitting parameters. Third, we fit the entire reflectance-versus-incident-angle data curve instead of focusing on only the critical angle region, which is just a small subset of the data. Finally, despite our use of highly scattering opaque samples, our experiment uniquely satisfies a key assumption behind the Mie scattering formalism, namely, no multiple scattering occurs. Further proof of our method's validity is given by the fact that our measured particle size finds good agreement with the value obtained by dynamic light scattering.

Following the same procedure as in section 1.4 we have obtained performed accurate particle sizing in the intralipid to within 7% compared to 39% for the traditional Fresnel theory as shown in table 5.2.

Model	$n_r$	$n_i(\times 10^{-4})$ ( $\alpha$ in $\text{cm}^{-1}$ )	MSD ( $\times 10^{-4}$ )	Mean particle diameter ( $\mu\text{m}$ )	Sizing error relative to DLS
AM	$1.36704 \pm 0.00001$	$33.7 \pm 0.3$ ( $642 \pm 5$ )	2.1	$0.3175 \pm 0.0019$	7%
F	$1.36704 \pm 0.00001$	$13.3 \pm 0.1$ ( $254 \pm 2$ )	4.1	$0.1820 \pm 0.0006$	39%

Table 5.2 The mean size for the suspended oil droplets extracted from our angle-dependent model (AM) is drastically different from the size obtained from traditional Fresnel theory (F). The size error in the last column is the percentage error compared to the size obtained from dynamic light scattering (DLS). The two models also differ significantly in their predictions for  $n_r$ ,  $n_i$ , and  $\alpha$ . DLS yields  $0.2962 \mu\text{m}$  for the particle size, within 7% of our result, but disagreeing with the F-model's prediction by almost 40%. Hence we trust our model's in situ sizing capability as well as its predictions for  $n_r$ ,  $n_i$ , and  $\alpha$ .



# Appendix A

## Controlling Temperature with Arduino

Arduino is a microcontroller based on the AMEL ATmega328P chip and contains a processor, 32kb of flash memory and a small amount of EEPROM and RAM memory. It interfaces with a host computer via USB. Using the open source Arduino software one can create and upload programs, also called “sketches” to the Arduino board. We will use the Arduino to monitor and control the temperature of the cell oven.

### The Circuit

The Arduino will sense the temperature of the cell oven by monitoring the voltage on a thermistor. Figure 5 shows the circuit diagram used to effectively convert the resistance of the thermistor to a voltage that is then sensed by the Arduino. The voltage on the thermistor will decrease with increasing temperature. The analog input of the Arduino saturates at five volts so  $R$  and the resistance on the potentiometer are chosen such that the output voltage is 4.9 volts at room temperature. Note that the thermistor must be calibrated before use. A step by step instruction how to calibrate the thermistor is described in the Electronic Instrumentation Laboratory manual [33]

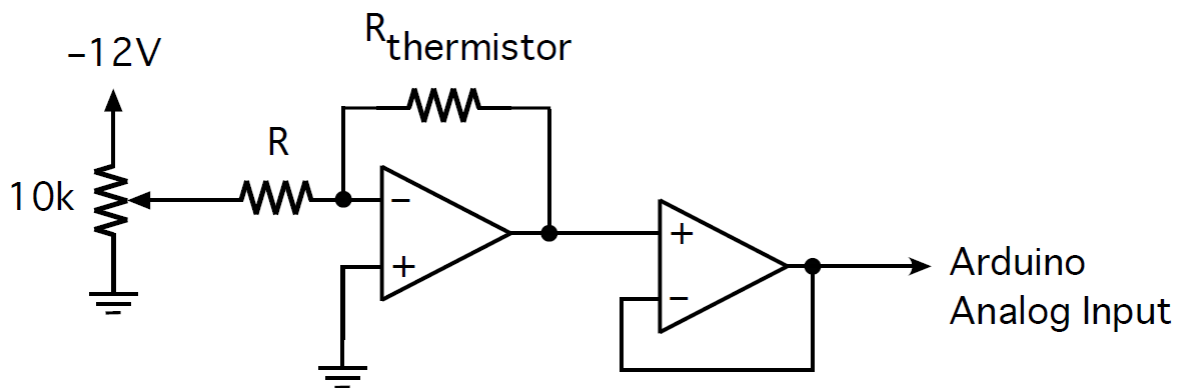


Figure A.1: Circuit diagram for connecting the thermistor to the Arduino. Reproduced from [33]

The next task the Arduino must do is turn the heating element on and off. A solid state relay is used in conjunction with the Arduino to accomplish this. As shown in figure 6 the solid state relay is connected to an outlet box used to powers the heater. Only when the relay’s control

input is “high”, between 3-5 volts, will the outlet supply power for the heater. When the Arduino outputs a high signal the oven will turn on and when it out puts a “low”, 0 volt, signal the heater will turn off. An image of the circuit used is shown in figure

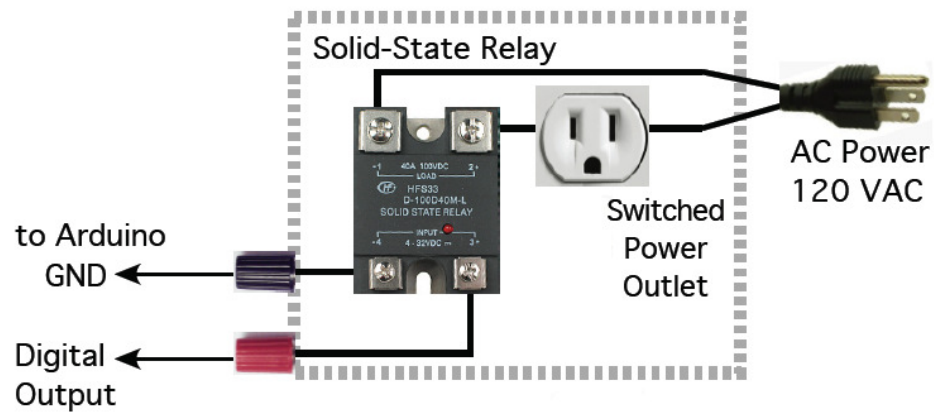


Figure A.2: Diagram depicting how the relay is used to control the power supply to heater. Reproduced from [33]

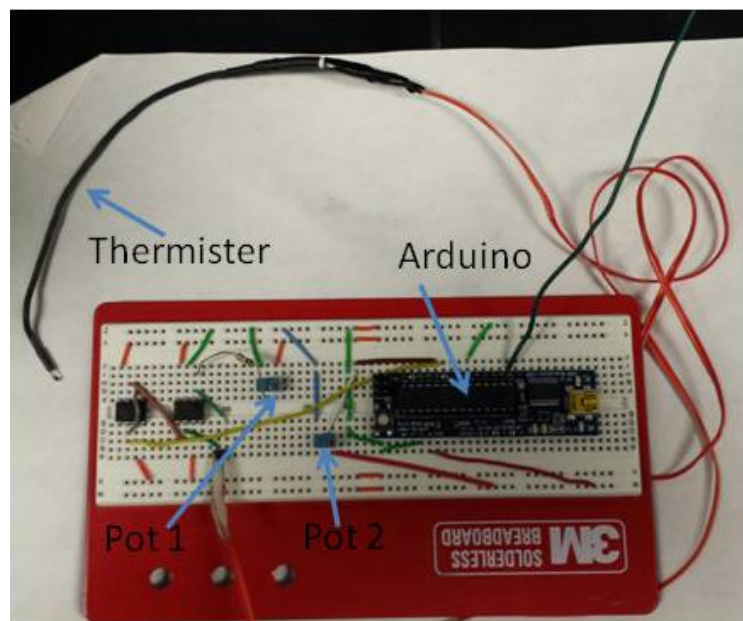


Figure 1 Image of the Arduino temperature controlling circuit. Note, Pot 1 is the potentiometer used in figure 5 and Pot 2 is used to set the temperature Arduino will maintain.

## Arduino sketch

Below is an annotated sketch that the Arduino will use to control the temperature of the cell oven. The first three lines define what pins the Arduino will use and I have redefined the name of the pin for ease of understanding the code. ThermPin is reading the voltage on the thermister. analogSetPin is the voltage across the wiper of a ten kilo ohm potentiometer where the pot is connected to five volts and ground. This allows the user to change the temperature of the oven without uploading a new sketch to the Arduino. The next two lines are variables which I have defined to be integers. The void setup loop simply tells Arduino that ThermPin and analogSetPin are both inputs and that it will be outputting digital signals to the digitalOutput pin. In the void loop the Arduino is constantly reading the voltage on the thermister and is constantly comparing that value to the value of the analogSetPin. When the voltage on the ThermPin is less than the analogSetPin the relay will receive a low input and the heater will be turned off. If the voltage on the ThermPin is greater than the analogSetPin then the relay will be high and the heater will be on.

```
const int ThermPin = A0;           //Thermister voltage
const int analogSetPin = A1;       //set temp Voltage
const int digitalOutput = 9;
int setVoltage ;                   //corresponds to lower temperature
int currentThermVoltage ;          // the voltage currently being measured

void setup()
{
  pinMode(ThermPin,INPUT);
  pinMode(analogSetPin,INPUT);
  pinMode(digitalOutput,OUTPUT);
  digitalWrite(digitalOutput,LOW);
}
void loop()
{
  currentThermVoltage = analogRead(ThermPin); // voltage read from thermister
```

```
setVoltage = analogRead(analogSetPin); //voltage set by user corresponds to set temp
if (currentThermVoltage < setVoltage){
//if the measured voltage is more than setVoltage
digitalWrite(digitalOutput, LOW);
//turn the heater off
}
if (currentThermVoltage >= setVoltage){
//if the measured voltage is less than setVoltage
digitalWrite(digitalOutput, HIGH);
//turn the heater on
}
}
```

## Refereed Publications as M.S. Co-Author

K. G. Goyal, M. L. Dong, V. M. Nguemaha, B. W. Worth, P. T. Judge, W. R. Calhoun, L. M. Bali, and S. Bali “Empirical Model of Total Internal Reflection from Highly Turbid Media” *Optics Letters* **38** 4888–4891, (2013)

M.L. Dong, K.G. Goyal, B.W. Worth, S.S. Makkar, W.R. Calhoun, L.M. Bali, and S. Bali “Accurate in situ measurement of complex refractive index and particle size in intralipid emulsions” *Journal of Biomedical Optics* **18**(8), 087003 (1-4) (2013)

K.G. Goyal, M. L. Dong, D. G. Kane, S. S. Makkar, B. W. Worth, L. M. Bali, and S. Bali “Refractive index sensing of turbid media by differentiation of the reflectance profile: Does error-correction work?” *Review of Scientific Instruments* **83**, 086107 (1-3) (2012)

## Oral Presentations at Miami University

- 1) “Ultra-Sensitive Magnetometry using Electromagnetically Induced Transparency: Can we produce “Slow Light”?”

*Talk by B.Worth at the Graduate Research Forum, Miami University (November 2013)*

- 2) “Investigation of electromagnetically induced transparency in an atomic vapor by a propagating laser beam: Effect of a transverse magnetic field”

*Talk by B.Worth at the Graduate Research Forum, Miami University (November 2012)*

# Bibliography

---

- [1] “Electromagnetically induced transparency-based slow and stored light in warm atoms”, I. Novikova, R. L. Walsworth, and Y. Xiao, *Lasers and Photonics Reviews* **6**, 333-353 (2012).
- [2] “Atomic clocks based on coherent population trapping: A review”, J. Vanier, *Applied Physics B* **81**, 421-442 (2005).
- [3] “Measurements of the magnetic field vector using multiple electromagnetically induced transparency resonances in Rb vapor”, K. Cox, V. I. Yudin, A. V. Taichenachev, I. Novikova, and E. E. Mikhailov, *Physical Review A* **83**, 015801 (2011).
- [4] “Vector magnetometry based on electromagnetically induced transparency in linearly polarized light”, V. I. Yudin, A. V. Taichenachev, Y. O. Dudin, V. L. Velichansky, A. S. Zibrov, and S. A. Zibrov, *Physical Review A* **82**, 033807 (1-7) (2010).
- [5] “Light speed reduction to 17 metres per second in an ultracold atomic gas”, L. V. Hau, S. E. Harris, Z. Dutton, and C. H. Behroozi, *Nature* **397**, 594-598 (1999).
- [6] “Slow, ultraslow, stored, and frozen light”, A. B. Matsko, O. Kocharovskaya, Y. Rostovtsev, G. R. Welch, A. S. Zibrov, and M. O. Scully, *Advances in Atomic, Molecular, and Optical Physics* **46**, 191-242, (2001).
- [7] “Photonics: Transparency on an optical chip” R. W. Boyd and D. J. Gauthier, *Nature* **441**, 701-702, (2006)
- [8] “Coherent effects on the Zeeman sublevels of hyperfine states in optical pumping of Rb by monomode diode laser” Y. Dancheva, G. Alzetta, S. Cartaleva, M. Taslakov, Ch. Andreeva *Optics Communications* **178** 103-110, (2000).
- [9] “Electromagnetically induced transparency in paraffin-coated vapor cells” M. Klein, M. Hohensee, D. F. Phillips, and R. L. Walsworth, *Physical Review A* **83**, 013826 (2011)
- [10] Irina Novikova, College of William & Mary, personal contact
- [11] J. Barkeloo, M.S. thesis, Miami University, 2012
- [12] A. Day, M.S. thesis, Miami University, 2013
- [13] “Switching from “absorption within transparency” to “transparency within transparency” in an electromagnetically induced absorption dominated transition”, K. Dahl, L. S. Molella, R. Rinkleff, and K. Danzmann, *Optics Letters*, **33** 983-985, (2008)

- 
- [14] “Pump-probe spectroscopy in degenerate two-level atoms with arbitrarily strong fields”, T. Zigdon, A.D Wilson-Gordon, and H. Friedmann, *Physical Review A*, **77**, 033836, (2008)
  - [15] Recently, sign reversal in vapor cells has been reported by varying the relative intensity of a pair of *linearly* polarized beams incident on the atomic sample [N. RAM, PhD thesis, Indian Institute of Technology Madras, 2011.]. Sign Reversal using linearly polarized beams was successfully created by Amanda Day recently (MS 2013) [REF?]. However, while there exists a clear theoretical model for describing sign reversal from circularly polarized beams [13], there exists no such model for explaining the sign reversal data from linearly polarized beams
  - [16] “Metamaterials a new frontier in science and technology” Y. Liu, X. Zhang *Chem. Soc. Rev.*, 2011,**40**, 2494–2507
  - [17] "Laser Diode Technology." *Newport Corporation*. N.p., n.d. Web. 2 Nov. 2013.  
<http://www.newport.com/Tutorial-Laser-Diode-Technology/852182/1033/content.aspx>
  - [18] “Saturated-absorption spectroscopy of weak-field Zeeman splittings in rubidium” J. Bowie, J. Boyce, and R. Chiao, *Optical Society of America* **12**, 1839-1842, (1995)
  - [19] “Notes on the Rb Maser and the CPT Clock”, D. Phillips,  
<https://www.cfa.harvard.edu/~dphil/work/rbmaser/masernotes.pdf> 2004
  - [20] M. Klein, Ph.D. thesis, Harvard University, 2009
  - [21] J. Lai, Z. Li, C. Wang, and A. He, *Appl. Opt.* **44**, 1845 (2005).
  - [22] S. Taylor, J. Czarnecki, and J. Masliyah, *Fuel* **80**, 2013 (2001).
  - [23] K. Alexander, A. Killey, G. H. Meeten, and M. Senior, *J. Chem. Soc. Far. Trans.* **77**, 361(1981).
  - [24] G. Meeten and A. North, *Meas. Sci. Tech.* **6**, 214 (1995).
  - [25] A. Reyes-Coronado, A. Garcia-Valenzuela, C. Sanchez-Perez, R. G. Barrera, *New J. Phys.* **7**, 89, 1 (2005).
  - [26] I. Niskanen, J. Rˆaty, and K-E. Peiponen, *Optics Letters* **32**, 862 (2007).
  - [27] K.G. Goyal, M. L. Dong, D. G. Kane, S. S. Makkar, B. W. Worth, L. M. Bali, and S. Bali “Refractive index sensing of turbid media by differentiation of the reflectance profile: Does error-correction work?” *Review of Scientific Instruments* **83**, 086107 (1-3) (2012)

- 
- [28] W.R Calhoun, H. Maeta, A. Combs, L. M Bali, and S. Bali *Optics letters* **45**,1224-1226 (2010)
- [29] M. C. Pena-Gomar, F. Castillo, A. Garcia-Valenzuela, R. G. Barrera, and E. Perez, *Appl Opt*, 45, 626-632 (2006)
- [30] M. McClimans, C. LaPlante, D. Bonner, and S. Bali, *Appl. Opt.* 45, 6477 (2006).
- [31] K. G. Goyal, M. L. Dong, V. M. Nguemaha, B. W. Worth, P. T. Judge, W. R. Calhoun, L. M.Bali, and S. Bali “Empirical Model of Total Internal Reflection from Highly Turbid Media”*Optics letters* **38** pp. 4888–4891, 10.1364 (2013)
- [32] M.L. Dong, K.G. Goyal, B.W. Worth, S.S. Makkar, W.R. Calhoun, L.M. Bali, and S. Bali “Accurate in situ measurement of complex refractive index and particle size in intralipid emulsions” *Journal of Biomedical Optics* **18(8)**, 087003 (1-4) (2013)
- [33] “Electronic Instrumentation Laboratory” J. Clayhold, H. Jaeger, M. Pechan, J. Priest Department of Physics Miami University Oxford, Ohio (2012)